SPECTROSCOPIC METALLICITY DETERMINATIONS FOR W UMa-TYPE BINARY STARS[*]

Slavek M. Rucinski[1], Theodor Pribulla[2], and Ján Budaj[2,3]

[1] Department of Astronomy and Astrophysics, University of Toronto, 50 St. George Street, Toronto, Ontario M5S 3H4, Canada; rucinski@astro.utoronto.ca
[2] Astronomical Institute, Slovak Academy of Sciences, 059 60 Tatranská Lomnica, Slovak Republic; pribulla@ta3.sk, budaj@ta3.sk
[3] Research School of Astronomy & Astrophysics, The Australian National University, Cotter Rd., Weston Creek, ACT, Australia 2611

ABSTRACT

This study is the first attempt to determine the metallicities of W UMa-type binary stars using spectroscopy. We analyzed about 4500 spectra collected at the David Dunlap Observatory. To circumvent problems caused by the extreme spectral line broadening and blending and by the relatively low quality of the data, all spectra were subject to the same broadening function (BF) processing to determine the combined line strength in the spectral window centered on the Mg I triplet between 5080 Å and 5285 Å. All individual integrated BFs were subsequently orbital-phase averaged to derive a single line-strength indicator for each star. The star sample was limited to 90 W UMa-type (EW) binaries with the strict phase-constancy of colors and without spectral contamination by spectroscopic companions. The best defined results were obtained for an F-type sub-sample ($0.32 < (B - V)_0 < 0.62$) of 52 binaries for which integrated BF strengths could be interpolated in the model atmosphere predictions. The logarithmic relative metallicities, [M/H], for the F-type sub-sample indicate metal abundances roughly similar to the solar metallicity, but with a large scatter which is partly due to combined random and systematic errors. Because of the occurrence of a systematic color trend resulting from inherent limitations in our approach, we were forced to set the absolute scale of metallicities to correspond to that derived from the m_1 index of the Strömgren $uvby$ photometry for 24 binaries of the F-type sub-sample. The trend-adjusted metallicities $[M/H]_1$ are distributed within $-0.65 < [M/H]_1 < +0.50$, with the spread reflecting genuine metallicity differences between stars. One half of the F-sub-sample binaries have $[M/H]_1$ within $-0.37 < [M/H]_1 < +0.10$, a median of -0.04 and a mean of -0.10, with a tail toward low metallicities, and a possible bias against very high metallicities. A parallel study of kinematic data, utilizing the most reliable and recently obtained proper motion and radial velocity data for 78 binaries of the full sample, shows that the F-type sub-sample binaries (44 stars with both velocities and metallicity determinations) have similar kinematic properties to solar-neighborhood, thin-disk dwarfs with space velocity component dispersions: $\sigma U = 33$ km s^{-1}, $\sigma V = 23$ km s^{-1} and $\sigma W = 14$ km s^{-1}. FU Dra with a large spatial velocity, $V_{\text{tot}} = 197$ km s^{-1} and $[M/H]_1 = -0.6 \pm 0.2$, appears to be the only thick-disk object in the F-type sub-sample. The kinematic data indicate that the F-type EW binaries are typical, thin-disk population stars with ages about 3–5.5 Gyr. The F-type binaries that appear to be older than the rest tend to have systematically smaller mass ratios than most of the EW binaries of the same period.

Key words: methods: observational – stars: abundances – techniques: spectroscopic

Online-only material: machine-readable and VO tables

1. INTRODUCTION

This investigation addresses heavy-element abundances (hereinafter called "metallicities") of W UMa-type eclipsing binary stars (hereinafter called EW systems). EW binary systems are defined as very close binary stars with orbital periods shorter than about 1 day,[4] consisting of solar-type (late-A to early-K) stars of identical surface temperature in spite of very different component masses. The mass ratios are observed to be always different from unity, down to 0.1 or even slightly less.[5] The definition of EW binaries based on the equality of surface temperatures bypasses the issue of the best theoretical model applicable to W UMa-type binaries. We also use the name "contact binary" because it is virtually impossible to equalize the surface temperatures of the disparate components without some form of a strong physical contact.

EW binaries are relatively common in the solar neighborhood with a frequency of about 1 per 500 FGK dwarfs (Rucinski 2006). Their ages are presumed to be rather advanced, which is inferred mostly from their occurrence along the main sequences of progressively older open (Kaluzny & Rucinski 1993; Rucinski 1998b) and globular (Rucinski 2000) clusters. It is generally assumed that the EW binaries form from moderately close binaries through angular-momentum-loss processes which take from a few hundred million to a few billion years. They are absent among young stars, with the youngest known in the open clusters Be 33 and Praesepe with estimated ages of 700 and 900 Myr (Rucinski 1998b). It is not clear if the main evolution channel is through evolutionary expansion of components in very close, but detached binaries, and to what extent this channel is augmented by shrinkage of the orbits due to the magnetic-wind induced angular momentum loss. Also, it is unknown if the mass ratio is reversed when the mass-exchange interaction takes place, although several arguments strongly point in this direction (Stepien 2006, 2009). In dense clusters, triple-body interactions may give an additional channel for the formation of EW binaries. We set all these problems and interpretations aside and

---

[*] Based on observations obtained at the David Dunlap Observatory, University of Toronto.
[4] The actual upper limit of the orbital period may be 1.3–1.5 days, as suggested by statistics for the galactic field data (Rucinski 1998a).
[5] We use the spectroscopic definition of the mass ratio defined to be less than unity, irrespectively of the depths of the respective eclipses. This matter is sometimes considered controversial for the "W-subtype" of the EW binaries for which less massive components appear to have slightly higher surface brightness. We disregard the photometric definition as irrelevant in our case.

concentrate on spectral observations to derive metallicities irrespectively of evolutionary mechanisms. We supplement these results by kinematic data which shed light on the most likely ages.

Stellar metallicities [M/H] are conventionally expressed as the fractional abundance of metals relative to hydrogen and expressed in logarithmic units relative to the Sun, [M/H] = $\log(M/H) - \log(M/H)_\odot$. EW binaries consist of solar-type stars with metallicities expected to be similar to those found among stars in the solar neighborhood. Any substantial chemical changes induced by evolution would be expected only for primaries of the most massive among EW progenitors and only for the CNO elements (to which our spectral window is blind); for the majority of the progenitors, the p–p cycle is not expected to modify the metal content. The only possibility of unusual chemical composition would be then through contamination by a highly processed material from a degenerate, currently invisible, but originally much more massive third star in the system. Thus, the derived metallicities are expected to reflect the properties of the EW progenitors even if mass-transfer takes place during their evolution. For galactic stars, metallicities are (weakly) correlated with ages (Reid et al. 2007; Feltzing & Bensby 2009) so that the results may shed light on the W UMa progenitor ages.

Kinematical properties of the solar-neighborhood stars are known to correlate with their age. The extensive study of the EW binaries by Bilir et al. (2005) was based on a sample of 129 objects with parallaxes and proper motions taken mostly from the *Hipparcos* satellite mission (European Space Agency 1997) and supplemented by center-of-mass radial velocities from the first nine papers of the David Dunlap Observatory (DDO) series (see Section 2). This sample—which was much more heterogeneous than that presented here through the inclusion of various other short-period binaries—suggests ages between a kinematically young (500 Myr) moving group to the age of the old galactic field population of about 5.5 Gyr. We re-address this matter by limiting the analysis to EW binaries of our spectroscopic sample and by using the center-of-mass velocities derived in the whole DDO survey, supplemented by new, improved reductions of the *Hipparcos* satellite proper-motion data.

Section 2 describes the spectroscopic observations of the DDO program while Section 3 discusses the use of the broadening functions (BFs) approach to derive integrated spectral line strengths. In Section 4 the strongest dependence of the strengths on the effective temperature is discussed. Determinations of metallicities [M/H] are given in Section 5; associated uncertainties in the determination process are discussed in Appendices A–C. Section 6 describes independent determinations utilizing the m_1 index of the Strömgren *uvby* photometry while Section 7 contains the results of an attempt to combine both methods of metallicity determinations. Section 8 discusses the space velocities of the binaries discussed in this paper. Section 9 places the results in the context of the evolution of EW binaries while Section 10 gives a summary of the paper and recommendations for further research.

2. THE STAR SAMPLE AND OBSERVATIONS

2.1. Definition of the Sample

The main data source for the present investigation is the spectroscopic radial velocity (RV) survey of close binaries conducted during the last decade of the DDO's existence, in the years 1998–2008. This survey consists of 15 main papers of the DDO RV analyses series. We give the list of all publications containing spectroscopic data for 163 binaries of the DDO survey in Table 1. In addition to the variable-star name, we give the "publication identification number" in the form (n:m), where n gives the DDO paper number and m is the star number in that paper.

All stars identified as W UMa-type or contact binaries in the DDO papers have been considered in the selection for metallicity determination. Three groups of EW binaries have been excluded from the current sample and are marked in Table 1.

All objects with components of dissimilar temperature as indicated by light curves known to show unequally deep eclipses. This investigation does not include objects with any indications of being semi-detached or with poor thermal contact. While this limitation was mainly related to the orbital-phase invariance of integrated BFs (to limit the continuum-normalization issues), it resulted in a more homogeneous and better defined sample. Besides, for binaries with components of unequal temperature, our technique of BFs would not provide consistent line-strength measurements. The excluded binary systems are marked in italics in Table 1.

Spectroscopically triple systems. The continuum normalization may be affected by the presence of a sharp-line companion as then its continuum and the pseudo-continuum of the binary do not add to unity in proportion to their luminosities; this prevents evaluation of correct respective line strengths. This effect was described in Rucinski (2010a), in the caption to Figure 17 of this paper; we discuss it in full in Appendix A.1. We excluded all EW binaries with third components contributing more than $\beta = L_3/L_{12} > 0.05$ to the observed spectra. The names of the rejected binaries are underlined in Table 1. Three binaries for which $\beta \leqslant 0.05$: HX UMa (8:8), SW Lac (10:5) and AG Vir (11:10); are marked by the slanted-cross (X) symbols in the figures of this paper. The high frequency of occurrence of companions to EW binaries is discussed in Pribulla & Rucinski (2006), D'Angelo et al. (2006), and Rucinski et al. (2007).

Binaries with poor data or lost original spectra. Two systems, V404 Peg (16:1) and HH Boo (16:3), had poor DDO data because of their faintness. For four binaries, LS Del (1:3), EF Dra (1:4), AP Leo (1:7), and UV Lyn (1:8) observed at the Dominion Astrophysical Observatory, Victoria, BC, we have been unable to acquire the original spectra for re-processing. The excluded binaries are marked by square brackets around their names in Table 1.

The DDO program included few detached and semi-detached binaries so the first of the above rejection criteria was applied automatically. However, to be able to say something about the detached binaries that do show the same temperatures at all phases, similarly as in the EW binaries, we included in this study two detached binaries, V753 Mon (3:9) and V1130 Tau (8:6). For stars close to the main sequence similarity of temperatures implies similarity of the masses. In this case, the mass ratios are, $q = 0.97$ and $q = 0.92$, respectively. These two binaries are marked in all figures by diamond symbols.

After the exclusions described above, the sample analyzed in this paper consists of 90 EW systems. Most of them (62 systems) are brighter than $V_{max} = 10$. The binaries which are fainter than $V_{max} \simeq 9.5$ frequently have poor standard photometry data and

Table 1
The DDO Spectroscopic Survey

D1	Binary Systems	Reference
0a	AH Vir	Lu & Rucinski (1993)
0b	*W Crv*	Rucinski & Lu (2000)
1	GZ And, V417 Aql, [LS Del], [EF Dra], V829 Her, FG Hya, [AP Leo], [UV Lyn], BB Peg, AQ Psc	Lu & Rucinski (1999)
2	AH Aur, CK Boo, DK Cyg, *SV Equ*, V842 Her, UZ Leo, XZ Leo, V839 Oph, GR Vir, NN Vir	Rucinski & Lu (1999)
3	*CN And*, HV Aqr, AO Cam, YY CrB, FU Dra[a], *RZ Dra*, UX Eri, RT LMi, V753 Mon, OU Ser	Rucinski & Lu (2000)
4	44 Boo, FI Boo, V2150 Cyg, V899 Her, EX Leo, VZ Lib, SW Lyn, V2377 Oph, *DV Psc*, *HT Vir*	Lu et al. (2001)
5	V376 And, EL Aqr, EF Boo, DN Cam, FN Cam, V776 Cas, SX Crv, V351 Peg, EQ Tau, *KZ Vir*	Rucinski et al. (2001)
6	*SV Cam*, EE Cet, KR Com, V401 Cyg, GM Dra, V972 Her, ET Leo, *FS Leo*, V2388 Oph, II UMa	Rucinski et al. (2002)
8	V410 Aur, V523 Cas, QW Gem, V921 Her, V2357 Oph, V1130 Tau, HN UMa, HX UMa, VY Sex, DZ Psc	Rucinski et al. (2003)
9	AB And, V402 Aur, V445 Cep, V2082 Cyg, BX Dra, V918 Her, V502 Oph, V1363 Ori, KP Peg, V335 Peg	Pych et al. (2004)
10	*V395 And*, *HS Aqr*, V449 Aur, FP Boo, SW Lac, *KS Peg*, IW Per, V592 Per, TU UMi, *FO Vir*	Rucinski et al. (2005)
11	DU Boo, *ET Boo*, TX Cnc, V1073 Cyg, *HL Dra*, *AK Her*, *VW LMi*, V566 Oph, *TV UMi*, AG Vir	Pribulla et al. (2006)
12	OO Aql, CC Com, V345 Gem, XY Leo, AM Leo, *V1010 Oph*, V2612 Oph, XX Sex, W UMa, *XY UMa*	Pribulla et al. (2007)
13	*EG Cep*, V1191 Cyg, V1003 Her, BD+7 3142, V357 Peg, V407 Peg, V1123 Tau, V1128 Tau, HH UMa, *PY Vir*	Rucinski et al. (2008)
14	TZ Boo, VW Boo, EL Boo, *VZ CVn*, *GK Cep*, RW Com, V2610 Oph, V1387 Ori, AU Ser, FT UMa	Pribulla et al. (2009b)
15	QX And, DY Cet, *MR Del*, HI Dra, *DD Mon*, V868 Mon, ER Ori, Y Sex	Pribulla et al. (2009a)
	TT Cet, AA Cet, CW Lyn, V563 Lyr, *CW Sge*, LV Vir, MW Vir, *GO Cyg*, V857 Her, *V752 Mon*, *V353 Peg*	incomplete orbits
16	[V404 Peg], V407 Peg[b], [HH Boo]	Maciejewski & Ligeza (2004)
17	*V471 Tau*	Kaminski et al. (2007)
18	AW UMa	Pribulla & Rucinski (2008)
19	GSC1387-475	Rucinski & Pribulla (2008)
20	*HD 73709, GSC 0814-0323*	Pribulla et al. (2009c)
21	*BX And, DO Cas, BV Eri, VV Cet, WZ Cyg*	Siwak et al. (2010)

Notes. The papers of the DDO series have numbers D1 between 1 and 15; additional papers included in the program have been assigned here arbitrary numbers outside the range 1–15. The paper DDO-7 (Rucinski 2002) is not listed here because it presented the method and a preliminary discussions at a mid-point of the DDO survey; it contained no data. Binaries excluded from the present study are marked in the table in three ways: in *italics* when non-contact, underlined when with a bright companion, $L_3/L_{12} > 0.05$, and in [square brackets] when the data were too poor to be used or the original spectra were lost.
[a] FU Dra: has also the variable-star name VX Dra.
[b] V407 Peg: more extensive data were published in DDO-13.

unreliable color-index information, a circumstance which had a potential impact on our analysis of metallicities (Section 4).

Practically all EW binaries analyzed in this survey fall into the spectral types interval between late-A to early-K types, i.e., with effective temperatures not higher than about 8500 K and not lower than about 4700 K. The luminosity classes had been found from the blue-region classification DDO spectra to correspond roughly to dwarfs (class V), although the luminosity class was usually very hard to evaluate from our spectra because of the complex appearance of broadened and blended lines. For the contact-binary geometry, the orbital period can be taken as a proxy of the component size; a spread of the orbital periods for a given temperature by less than about 50%–70% indicates that some components may be moderately evolved, but generally still within the width of the main sequence (Rucinski & Duerbeck 1997; Rucinski 1998b).

2.2. The Spectroscopic Material

The spectral window used during the DDO RV program was centered on the 5184 Å line of the neutral magnesium triplet "b" at 5167.32, 5172.68, and 5183.60 Å. The triplet region was found to be very convenient for RV measurements for most EW systems observed at DDO because of its sufficient strength for all spectral types later than about A2V–A4V down to the latest spectral-type EW binaries that we observed. For the F2V template spectrum that we used, the strongest line in the spectral window was actually not a Mg I triplet line, but the line Fe II at 5169 Å (see Table 2 and Section 3.2). In terms of the summed strength of the absorption lines in the spectral window in the F2V spectrum, this line contributes about 8%, while all

three lines of the Mg I triplet contribute about 7%. These proportions rapidly change with the spectral type as the magnesium triplet becomes stronger relative to iron lines for lower temperatures.

The width of the actual spectral window that was used during the DDO spectral survey changed depending on the combination of the available CCD detector and the diffraction grating. The spectral resolving power of the spectra varied within $R = 10,000$–$17,000$, depending on the (nightly) selectable slit width and the grating. Typical signal-to-noise ratio (S/N) values were at a level of 10–50. For the current investigation, we utilized the one-dimensional, rectified spectra of the RV program. However, for the sake of uniformity of the material, we undertook a major re-determination of all, over 4500 BFs for the same spectral window (5080–5285 Å) and at the same resolution of 11.8 km s^{-1} pixel^{-1}. During this exercise, we addressed the quality of the spectra and rejected spectra which had been given low weight in the RV program. The total material consisted of 4531 spectra for 90 binaries; after all rejections, this was reduced to a total of 4333 spectra, hence on average 48 spectra per star.

3. BF INTEGRALS AS METALLICITY INDICATORS

3.1. The Broadening Functions Technique

Stellar metallicities are usually determined using high S/N and high-resolution spectra. With rotational velocities of individual components typically $V \sin i > 100$–150 km s^{-1}, and with blended profiles of both components frequently exceeding 600 km s^{-1}, the EW binaries are very difficult targets for spectral studies. There is no hope of contemplating any

Table 2
Spectral Lines in the Window 5080–5285 Å

λ (Å)	El.ion	W (mÅ)
5110.413	Fe I	80
5133.681	Fe I	85
5139.251	Fe I	89
5139.462	Fe I	95
5142.927	Fe I	98
5162.292	Fe I	82
5165.407	Fe I	80
5167.321	Mg I	135
5167.487	Fe I	112
5169.033	Fe II	853
5171.595	Fe I	99
5172.684	Mg I	270
5183.604	Mg I	356
5188.680	Ti II	96
5191.455	Fe I	92
5192.343	Fe I	96
5194.941	Fe I	89
5195.468	Fe I	81
5197.577	Fe II	100
5202.335	Fe I	80
5204.506	Cr I	100
5206.038	Cr I	105
5208.419	Cr I	109
5216.274	Fe I	86
5226.543	Ti II	94
5226.862	Fe I	92
5227.150	Fe I	93
5227.189	Fe I	118
5232.939	Fe I	106
5234.625	Fe II	103
5239.813	Sc II	112
5258.842	Si I	84
5265.556	Ca I	80
5266.555	Fe I	98
5269.537	Fe I	126
5270.270	Ca I	89
5270.357	Fe I	105
5276.002	Fe II	107
5281.700	Fe I	83
5283.621	Fe I	90

Note. The equivalent widths W of the lines with $W >$ 80 mÅ for a model atmosphere approximating the template, HD 128167, with $T_{\rm eff} = 7000$ K and $\log g = 4.5$.

traditional approach in determination of metallicities and ever observing individual lines in the optical-region spectra of EW binaries. Reliable techniques of RV determinations based on cross-correlation or linear deconvolution have been developed only within the last few decades. However, RV determinations are much less demanding on the quality of spectra than studies of chemical content because they are based on simultaneous RV *shifts* (but not strengths) of many spectral lines. All papers of the DDO series used the BF approach (Rucinski 2002). The BF approach is superior to the cross-correlation because it is a linear deconvolution process and thus gives directly interpretable results without any need for additional calibration.

Here we use the BF strength somewhat similarly to the concept of the equivalent width: the integral of the BF function represents the combined strengths for all lines within the spectral window. The BF integrals were averaged in the temporal (orbital phase) domain. Thus, we utilize integration and averaging to

extract the information on the line strength from the low S/N, heavily broadened and blended spectra.

The BFs deconvolution process was described in Rucinski (1992, 2002, 2012) and then extensively used in all papers of the DDO series. It is very similar to the least squares deconvolution method introduced by Donati & Collier Cameron (1997) and Donati et al. (1997), but utilizes a stellar spectrum template rather than a model spectrum. This choice was made (1) to directly relate radial velocities of the DDO survey to the RV standards, (2) to have template and program spectra affected by the same instrumental effects, and (3) to include all spectral lines, even the weakest ones, which could be missed in model spectra.

3.2. Synopsis of the Metallicity Determination

Derivation of the BF integrals, hereinafter called S, and metallicity involves several steps and assumptions.

The spectral template. From among about a dozen template stars used during the DDO RV survey, we selected the frequently observed HD 128167 (σ Boo, HIP 71284, F2V). Its rotational velocity is well below the resolution of our spectrograph of about 20 km s^{-1}, with measured values of $V \sin i$: 9.3 km s^{-1} (Valenti & Fischer 2005), 7.7 km s^{-1} (Schroder et al. 2009), and 7.32 km s^{-1} (Martinez-Arnaiz et al. 2010). HD 128167 permitted the best coverage of the whole range of the observed spectral types and $B - V$ colors in the sense that the values of S were rather uniformly distributed around unity. When the spectral types and metallicities of a program object and of the template match perfectly, the S integral should be equal to unity; a mismatch in the effective temperatures has the strongest effect on S. Note that the template star actually appears to show some metal under-abundance with [M/H] = −0.38 (Valenti & Fischer 2005), although this is unimportant because the template spectrum was used only as an intermediate device in the BF determination process. The template spectrum obtained by averaging of several individual spectra was very well defined and due to star's low rotational velocity, we did not encounter any problems with the continuum rectification as with the binary targets.

Measurements of the strength. Each rectified spectrum of the DDO program was deconvolved with the template spectrum producing one BF function which was subsequently integrated above the local baseline to provide one value of S. As is shown in an example in Figure 1, the BF baseline was typically shifted vertically by the (usually slightly negative) value δ. Such shifts represent missing information on the real continuum level; in the spectral domain the corresponding shifts are denoted Δ below. In an idealized case of the perfect spectral match of the program and template spectra, and thanks to the linear properties of the BF's, the integral of the BF above the baseline should correctly represent the combined strength of the lines within the spectral window. Then, a rectification step involving a shift by Δ would produce *linear* scaling of S by $(1 + \Delta)$, where Δ should be determinable from δ. As we describe in Appendix A, we were not successful in our attempts to use the values of δ to derive Δ in individual cases, but we could still use *the observed range in δ to estimate the expected range of systematic errors* in the measurements of S.

Averaging of the BF strengths in phase. This step allowed us to check on the constancy of the line strengths in phase,

to ascertain the invariability of the apparent T_{eff} and thus to confirm the EW type of the binary. Subsequently, individual values of S were averaged with a 2.5σ clipping which led to rejection of 4% of all spectra. None of the binaries of the final sample of 90 binaries showed any phase dependence in S.

Effective temperatures and colors. The effective temperature T_{eff} plays a crucial role because S is very strongly dependent on it. Additionally, for contact binaries, many stellar properties correlate with T_{eff}. For practical reasons, we used the de-reddened color index $(B-V)_0$ as a proxy for T_{eff}. Derivation of the $B-V$ colors and interstellar reddening corrections is described in Section 4.

Calibration using model spectra. The strengths of spectral lines as well as S values depend on the atmospheric properties of the star, i.e., the effective temperature, T_{eff}, the surface gravity, $\log g$, and the metallicity, [M/H] ($S = S(T_{\mathrm{eff}}, \log g, [\mathrm{M/H}])$). The dependence is strongest on T_{eff} and is much weaker on $\log g$ and on [M/H]. While the model values of S were found for two values of gravity, $\log g = 3.5$ and 4.5 (cgs), the weak dependence on g led us to use S only for $\log g = 4.5$, but with the proper account in the final error budget (see Section 5.1 and Appendix A.2). For comparisons with the observations, the T_{eff} dependence was transformed into the $B-V$ color-index dependence, as discussed in Section 4. Note that the same template spectrum was used for both the observed and model spectra, so that the template served only in the process of converting the spectra into the BFs with no direct influence of its properties on the final results.

Derivation of metallicities. The [M/H] values were found by interpolation in the pre-computed table of the BF integrals $\log S = \log S(T_{\mathrm{eff}}, [\mathrm{M/H}])$ for one value of $\log g = 4.5$, but taking into account the range of gravities in the error budget. We used two-dimensional interpolation utilizing the observed, reddening-corrected values $(B-V)_0$ and the measured, average values of $\log S$. We used $\log S$ instead of the combined line strength S in anticipation of a need for scaling which would show up as an additive shift rather than a multiplying factor. The curve of growth (dependence of the equivalent width on the abundance) has almost linear regions in logarithmic units which is an advantage when interpolation is used. Uncertainties and the error budget of metallicity determinations are discussed in detail in Appendix A.

4. EFFECTIVE TEMPERATURE

4.1. B − V Index Data

The effective temperature of a star is the most important independent parameter in the spectral line-strength analysis. For EW binaries, it is the parameter known to correlate with most of their astrophysical properties like for objects distributed along the main sequence. The most obvious and simplest indicator of the effective temperature would be the spectral type. Unfortunately, spectral classification—which we attempted to provide in most of the DDO-series papers using the blue-region, low-resolution spectra—is a very unreliable tool when applied to EW binaries. The large widths of spectral lines and the general washed-out appearance of spectra compared with FGK-type spectral standards make spectral typing uncertain. At best, the spectral type can be estimated to two or three spectral subtypes.
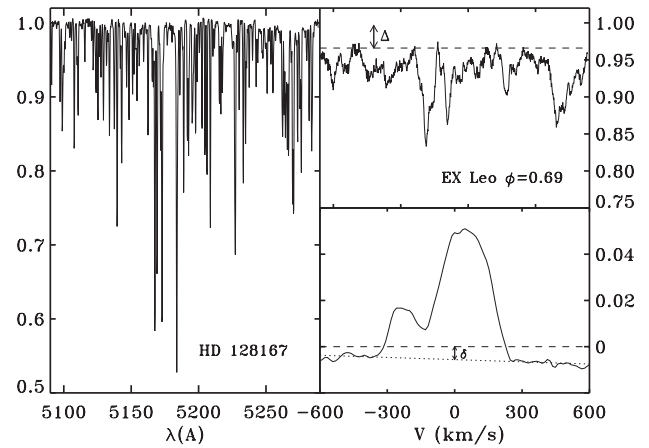

Figure 1. Typical template and program spectra and the resulting BF. The left panel shows the template spectrum (HD 128167), while the right panel shows one of program spectra, here of EX Leo (4:5), at the orbital phase 0.69. The corresponding BF is plotted below. Note the negative shift in the BF baseline (δ) which is the result of spectral rectification to the pseudo-continuum rather than to the real continuum. The integral of the BF above the baseline, S, is the quantity used to derive metallicities.

Systematic errors in spectral classification for EW binaries are entirely unknown.

The situation is not much better with color-index data, mainly because literature data are very inhomogeneous or sometimes simply lacking. Unfortunately, many light curves for EWs were obtained in instrumental systems without any attempts at standard-system calibration. There have been few studies aimed at providing calibrated $B-V$ or $b-y$ indices from observations at random orbital phases. Even a few such observations are useful because the orbital color variations for genuine W UMa-type systems are small, typically by less than 0.02–0.03 in $B-V$. This circumstance simplifies the derivation of mean color indices although it prevents reduction of errors of such mean colors to less than about 0.01–0.02.

The $B-V$ color index was used as the temperature indicator in this investigation. The main source of uniformly calibrated mean $B-V$ indices was Terrell et al. (2012) who obtained random $BVRI$ measurements specifically to improve the homogeneity of the EW binary photometric data. Their survey includes binaries fainter than $V \simeq 9$ of which 42 are among the objects analyzed in this paper. We adopted the *Tycho-2* (European Space Agency 1997) colors for the remaining binaries of the sample. The colors derived from the *Tycho-2* project have the advantage of uniformity in calibration over data gleaned from literature. The colors were obtained from the mean instrumental *Tycho-2* magnitudes B_T and V_T, transformed to the colors: $B - V = 0.85\,(B_T - V_T)$. The uncertainties of the $B-V$ colors are much smaller than formal errors of mean magnitudes would imply because the latter include stellar variability; they are typically at a level of about 0.01 mag, but deteriorate rapidly beyond a B_T of around 9.5 mag. The adopted values of $B-V$ are listed in Table 3.

The $B-V$ index can be estimated from $b-y$ observations of EW binaries available in the literature. The EW binaries were observed in the Strömgren photometric system by Hilditch & Hill (1975), Rucinski & Kaluzny (1981) and Rucinski (1983). Additional studies which included EW binaries within larger photometric programs are cited in Section 6. The *uvby* data have the advantage over the literature $B-V$ values of superior accuracy thanks to the well-defined and more rigorous calibration procedures. While we did not use the $b-y$ colors

Table 3
Basic Assumed Parameters for the Analyzed EW Binaries

D1:D2	Name	Period (day)	V_{max}	$B - V$	$E(B - V)$	d (pc)
1:1	GZ And	0.3050	10.85	[1.12 ± 0.10]	0.03	160 ± 32
1:2	V417 Aql	0.3703	10.62	0.64 ± 0.01	0.05	200 ± 40
1:5	V829 Her	0.3582	10.39	0.65 ± 0.04	0.01	210 ± 42
1:6	FG Hya	0.3278	10.00	0.62 ± 0.01	0.01	200 ± 40
1:9	BB Peg	0.3615	10.97	[0.48 ± 0.01]	0.00	290 ± 58
1:10	AQ Psc	0.4756	8.66	[0.47 ± 0.01]	0.04	150 ± 23
2:1	AH Aur	0.4943	10.18	0.64 ± 0.01	0.03	110 ± 22
2:2	CK Boo	0.3552	9.09	0.52 ± 0.01	0.02	120 ± 24
2:3	DK Cyg	0.4707	10.47	0.38 ± 0.01	0.03	120 ± 24
2:5	V842 Her	0.4190	9.98	0.67 ± 0.04	0.02	240 ± 48

Notes. The publication identification number D1:D2 uses the paper number D1 (see Table 1) and the successive number D2 within the paper. The photometric data V_{max}, $B - V$ and $E(B - V)$ and the distances (d) have been estimated as described in the text. The $B - V$ colors taken from the *Tycho-2* Catalog (European Space Agency 1997) are given in square brackets.

(This table is available in its entirety in machine-readable and Virtual Observatory (VO) forms in the online journal. A portion is shown here for guidance regarding its form and content.)

directly, their agreement with the adopted $B - V$ data was used for evaluation of the uncertainties of $B - V$.

Interpretation of our spectroscopic data on metallicities required reddening-corrected $(B - V)_0$ colors; the reddening corrections are described in the next Section 4.2. The errors of the $(B - V)_0$ colors have been estimated as resulting from three sources: (1) the scatter in the measured $B - V$; (2) inconsistencies with spectral types estimated independently during the DDO program; (3) uncertainties in the reddening corrections. They are listed in Table 3 with the observed mean $B - V$ and the reddening corrections $E(B - V)$.

An attempt was made to use an infrared color index in addition to $B - V$. The infrared observations are expected to give better estimates of effective temperatures than $B - V$ because they are less affected by interstellar reddening. The Two Micron All Sky Survey (2MASS) project (Skrutskie et al. 2006) provided single-epoch, simultaneous observations in the J, H and K bands. The longest-base index $J - K$ can serve as an useful effective-temperature indicator for late-type stars; it is metallicity independent and is weakly dependent on interstellar reddening with $E(J - K) \simeq 0.5 \times E(B - V)$. We found that the *2MASS* data are not sufficiently precise for our purpose: they have errors at a level of typically 0.03, but with large scatter in between stars. Generally, the reddening-corrected values of $(J - K)_0$ agreed with $(B - V)_0$ values, but we also noted large discrepancies for some objects which could be mostly traced to individual poor $J - K$ measurements.

4.2. Interstellar Reddening

Most of the EW binaries of this study lie in the distance range 15–500 pc; the resulting reddening corrections $E(B - V)$ in $(B - V)_0 = (B - V) - E(B - V)$ are generally small. Because of the very clumpy nature of the interstellar matter in the galactic disk, accurate (better than <0.01 mag) values of $E(B - V)$ are relatively difficult to estimate; they become relatively more predictable at large distances through averaging in many individual clouds.

We attempted to account for the nonuniform distribution of the dust clouds in the Galaxy in the following way: rather than using a model with one number characterizing $E(B - V)$ per unit of distance, we utilized as primary information the

maximum reddening correction in a given galactic direction, as seen throughout the whole Galaxy. Such maximum values were then scaled down by the estimated distance to the object assuming a finite thickness of the galactic dust layer. The values of $E_{max}(l, b)$, interpolated from the maps of Schlegel et al. (1998), were found using the IDL routines provided by these authors.[6] Such maximum reddening values typically ranged between 0.02 at the galactic poles to large values of several magnitudes in the galactic plane. The assumed values of $E(B - V)$ were then derived by scaling $E_{max}(l, b)$ by the length of the path to the binary within a dust slab of semi-thickness of 150 pc: $E(B - V) = E_{max}(l, b) \times \min(1, d \sin(b)/150)$. The distances d were estimated in three different ways and then inter-compared to provide best estimates (given in Table 3) using: (1) new determinations of the *Hipparcos* parallaxes (van Leeuwen 2007); (2) the color-independent calibration, $M_V = -1.5 - 12 \log P$, which applies to short-period EW's with $P < 0.56$ days (Rucinski 2006); and (3) the color and reddening-dependent calibration, $M_V = -4.44 \log P + 3.02 (B - V)_0 + 0.12$, requiring a single-step iteration in the reddening-corrected color (Rucinski & Duerbeck 1997).

The values of EBV determined in the above way have a (relatively small) median of 0.027. Additional checks on the amount of reddening were possible for objects within 30 pc using interstellar polarization data (Leroy 1999) and the gas column density for the Na I D-line (Lallement et al. 2003) and O VI (Oegerle et al. 2005) interstellar lines, but no discrepancies from the previously determined values larger than 0.01 were noted.

The reddening corrections were adjusted for two binaries, V1191 Cyg (13:2) and OO Aql (12:1), with the latter so uncertain that OO Aql has been excluded from the metallicity analysis (Section 5.3).[7] We list the adopted $B - V$ colors and

---

6 http://www.astro.princeton.edu/~schlegel/dust/index.html
7 For V1191 Cyg, we used $E(B - V) = 0.12$, based on the comparison of the observed color with the spectral type. OO Aql (12:1) has been recognized as an unusual object with the red color being due to its low temperature (Mochnacki 1981; Hrivnak 1989), but the DDO observations (Pribulla et al. 2007) gave masses that were too large for a K-type binary; the spectral corresponding to the total mass is F8V. We assumed $E(B - V) = 0.16$, which is much larger than the 0.07 predicted from the sky position and assumed distance. Reddening is very clumpy in this area of the sky; a value as large as $E(B - V) \simeq 0.20$ is not excluded.

Table 4
Model Atmosphere Values of log S

$B-V$	-2.0	-1.5	-1.0	-0.5	0.0	$+0.5$	$\Delta_g \log S$
0.00	-1.286	-1.038	-0.820	-0.620	-0.428	-0.232	-0.028
0.10	-1.037	-0.807	-0.602	-0.418	-0.252	-0.099	-0.019
0.20	-0.805	-0.591	-0.402	-0.237	-0.095	0.023	-0.010
0.30	-0.591	-0.393	-0.221	-0.075	0.043	0.132	-0.010
0.40	-0.396	-0.212	-0.058	0.067	0.163	0.228	-0.014
0.50	-0.220	-0.050	0.086	0.190	0.265	0.313	-0.024
0.60	-0.064	0.092	0.210	0.294	0.350	0.384	-0.031
0.70	0.072	0.214	0.313	0.379	0.419	0.443	-0.036
0.80	0.188	0.314	0.397	0.446	0.473	0.489	-0.033
0.90	0.282	0.392	0.459	0.495	0.512	0.522	-0.026
1.00	0.355	0.447	0.500	0.526	0.536	0.542	-0.015
1.10	0.407	0.478	0.520	0.539	0.546	0.549	-0.006
1.20	0.436	0.484	0.520	0.539	0.546	0.549	-0.002

Notes. The table lists the model values of log S for log $g = 4.5$ and for the values of [M/H] as given in the column headers labeled -2.0 to $+0.5$. The median differences in log S (for all metallicities) between log S for log $g = +3.5$ and $+4.5$, scaled to $\Delta \log g = 0.3$, are given in the last column.

reddening estimates in Table 3. We note that the reddening corrections, even if small, affect not only the $(B-V)_0$ colors, but also the Strömgren photometry indices m_1 which were used for comparison and calibration of our metallicity determinations (Section 6).

5. DETERMINATION OF METALLICITIES

5.1. Model Spectra

A grid of synthetic spectra covering the 5070–5300 Å was computed using the code Synspec (Hubeny & Lanz 1995; Krtička 1998) with the structural variables of the model atmospheres (depth dependences of the state variables) adopted from Castelli & Kurucz (2004). The models assume LTE, radiative and hydrostatic equilibrium with convection, and a plane-parallel geometry. The grid was defined by 11 temperature, 2 gravity, and 6 metallicity values, with 1 value of microturbulence of 2 km s^{-1}. The effective temperatures, $T_{\rm eff}$, varied from 4000 K to 9000 K in steps of 500 K. The two values of the surface gravity were log $g = 3.5$ and log $g = 4.5$ (cgs) while the metallicity, [M/H], varied from -2.0 to $+0.5$ in steps of 0.5 (i.e., metal abundances ranging from 0.01 solar to $3\times$ solar). The abundances of all elements (except of H, He) were varied in the same proportion relative to the hydrogen abundance. The spectra were calculated with a wavelength step of 0.01 Å or about 0.6 km s^{-1} for our spectral window.

The synthetic spectra were prepared for use with the observed BF strengths S by the following transformations: (1) we convolved them with a Gaussian profile with $\sigma = 15$ km s^{-1} to avoid problems with model spectra having shaper lines than for the template, (2) we sampled the resulting spectra to the same resolution as the observational spectra (11.8 km s^{-1} pixel^{-1}), and (3) we determined the BFs and their strengths for the observational spectral window 5080–5285 Å using the same stellar spectrum template HD 128167.

The tables of log $S_{\rm th}(T_{\rm eff}, [M/H])$ were computed for the two model values of log g, but we used only those for log $g = 4.5$ (cgs). Table 4 lists the values of log $S_{\rm th}$ for the observational $B-V$ scale of Bessell, as is more fully described in the next Section 5.2. The influence of the gravity difference between log $g = 3.5$ and 4.5 is not negligible and has been taken into account by including a term in the total error budget

(see Appendix A.2). In principle, we could determine gravities for individual W UMa binaries, but this would require us to provide combined photometric (light curve) and spectroscopic (radial velocities) solutions which we tried to avoid. While we do have new RV solutions for all binaries of the survey, lack of photometric data would eliminate some systems and the combined solutions would have to include new, photometric-model dependent uncertainties.

5.2. Synthetic $B-V$ Colors

The same atmosphere models used for the computation of the high-resolution synthetic spectra for the Mg I window were used to calculate theoretical values of the $B-V$ color indices using the filter transmission curves of the Johnson system (Johnson & Morgan 1951), and the zero points for the magnitude system as described in Budaj et al. (2005). The theoretical $B-V$ indices obtained from the model atmospheres are metallicity dependent through the changes of opacity accompanying changes of [M/H]. This dependence is important because it couples with the direct metallicity dependence of the integrated line strength S on the temperature. We took it into account by interpolating the model values of log S for each metallicity into the common, solar-metallicity $B-V$ scale.

We compared our $T_{\rm eff}$, $B-V$ calibration with the observational calibration of Bessell (1979) for the solar abundance. The differences in $\Delta(B-V)$, in the sense (Bessell: present models), are shown in Figure 2. We applied the same differences to our model $B-V$ results for all metallicities assigning them to imperfections in filter transformations. They represent an inherent (systematic) uncertainty in the models and will reflect in uncertainties of [M/H] which we denote as ϵ_4 (see Appendix A.2).

5.3. Metallicities from log S

Table 3 lists the observational data assumed for metallicity determination, Table 4 gives the model predictions and Table 5 lists the integrated BF line strengths log S of individual stars. Figure 3 shows the values of log S plotted on top of the model atmosphere results; the data points with error bars represent the measured values while the model results are shown by dotted lines. The general impression is of a good agreement with the solar-metallicity models. The two detached binaries with identical components and the three triple systems with faint

Table 5
Measured Combined Line Strengths and Metallicities

D1:D2	Name	Gr	m	$\log S$	$\epsilon(\log S)$	$\delta \times 10^3$	[M/H]	[M/H]$_m$	[M/H]$_1$	ϵ[M/H]
1:1	GZ And	R	26	0.394 ± 0.004	0.100	−0.95 ± 0.29	[−2.03]	...	[−0.52]	[0.28]
1:2	V417 Aql	F	22	0.229 ± 0.007	0.076	−0.20 ± 0.27	−0.84	−0.46	−0.46	0.19
1:5	V829 Her	R	4	0.249 ± 0.015	0.082	−2.24 ± 0.43	−0.90	...	−0.43	0.21
1:6	FG Hya	F	30	0.257 ± 0.005	0.074	−2.68 ± 0.17	−0.67	−0.14	−0.26	0.19
1:9	BB Peg	F	28	0.298 ± 0.006	0.058	−0.13 ± 0.27	[0.51]	...	[0.63]	[0.15]
1:10	AQ Psc	F	37	0.202 ± 0.003	0.056	−2.56 ± 0.07	0.18	...	0.18	0.14
2:1	AH Aur	F	32	0.296 ± 0.004	0.077	−2.55 ± 0.16	−0.41	0.08	0.00	0.19
2:2	CK Boo	F	28	0.179 ± 0.004	0.061	−2.04 ± 0.14	−0.49	...	−0.33	0.15
2:3	DK Cyg	F	27	0.016 ± 0.005	0.041	1.12 ± 0.16	−0.42	−0.26	−0.61	0.10
2:5	V842 Her	R	26	0.324 ± 0.006	0.083	−2.95 ± 0.20	−0.42	...	0.08	0.22

Notes. Column headings are as in Table 3 with the additional headings D1:D2: binary identification; Gr: the group to which the binary belongs: B for blue $((B-V)_0 \leqslant 0.32)$, F for F-type $(0.32 < (B-V)_0 \leqslant 0.62)$, and R for red $((B-V)_0 > 0.62)$; m: the number of phase points used for averaging of independent orbital points; $\log S$: the mean broadening function strength with its observational error (ϵ_1) evaluated from the phase scatter; $\epsilon(\log S)$: the assumed, combined error of $\log S$ consisting of five components, as described in Appendix A.3; δ: the measured shift in the BF baseline with its error, both multiplied by 10^3 for more convenient formatting. The metallicities: the raw determination [M/H], the metallicity derived from the Strömgren m_1 index [M/H]$_m$, the trend-corrected [M/H]$_1$ and the assumed final error ϵ[M/H]. Metallicities determined through extrapolation beyond the model grid and thus entirely unreliable are given in square brackets (see the text).

(This table is available in its entirety in machine-readable and Virtual Observatory (VO) forms in the online journal. A portion is shown here for guidance regarding its form and content.)
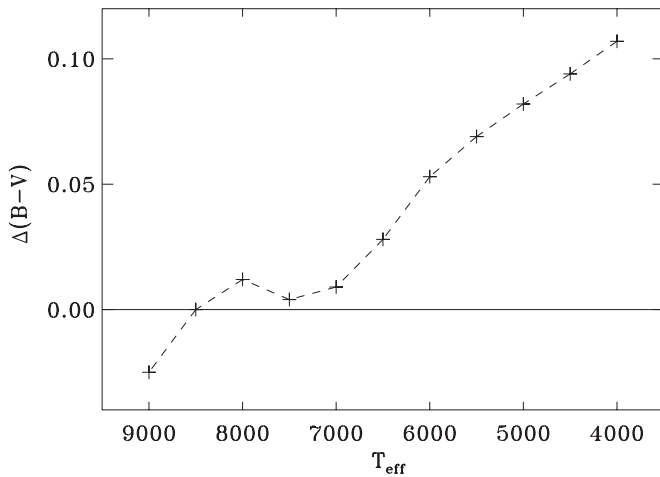

Figure 2. Differences between $B-V$ values from the Bessell (1979) calibration and our model results, plotted vs. the model effective temperature for the solar metallicity and $\log g = 4.5$. We used these color differences as one of indicators of systematic uncertainties in the combined line-strength estimates (ϵ_4).

Figure 3. Observed values of the BF integrals, $\log S$ (error bar symbols), over-plotted on the model results (lines) for $\log g = 4.5$. The observational line strengths have been corrected for the baseline displacements δ, as described in Appendix A.1. The dotted lines correspond to model results for metallicities [M/H] in intervals of 0.5 between −2 and +0.5; the solar case is shown by the solid line. In this and the following figures, the two detached binaries are marked by the open rhombus symbols while the three triple systems with $L_3/L_{12} < 0.05$ are marked by X symbols. The error bars for $(B-V)_0$ and $\log S$ do not take into account uncertainties in the model atmospheres and correspond to the quadratically added ϵ_1 and ϵ_2 only.

companions do not appear to deviate much from the general, solar-metallicity dependence and seem to merge within the general scatter of the data.

Note that Figure 3 does not present *metallicity determinations*; the results only suggest a general agreement with the assumption of the solar metallicity with [M/H] within roughly ±0.5. Determination of [M/H] requires a detailed comparison with the atmosphere models, with all model uncertainties, and is more complex than what can be directly inferred from Figure 3.

The model predictions of the integrated line strengths $\log S$ (dotted lines in Figure 3) form a smooth and simple two-dimensional function $\log S = f((B-V)_0, [M/H])$. As expected, the strengths $\log S$ depend monotonically on [M/H] and on $B-V$. They tend to saturate for red stars and for positive values of [M/H]. This simple monotonic shape of the model function f permits its inversion into a function [M/H] $= F((B-V)_0, \log S)$ to use for determination of [M/H]. However, such an inversion is constrained by the tendency for saturation at red colors and large values of [M/H]. Besides,
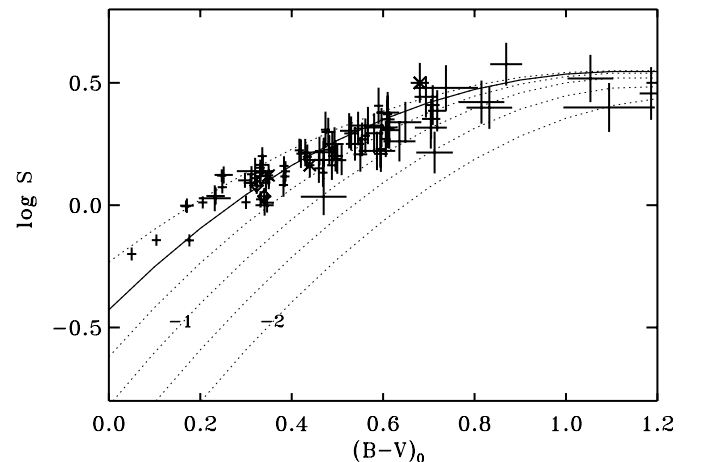
determination of [M/H] requires that uncertainties in the model function are taken into account, in addition to uncertainties in the observational data. Such systematic errors, denoted as ϵ_3 and ϵ_4 and the related quasi-random error ϵ_5, are discussed in Appendix A.3.

The individual values of [M/H] obtained by bi-linear interpolation in the model data are shown in Figure 4. The EW binaries appear to have metallicities very roughly solar, but with systematic and significant deviations.

1. Some binaries occupy the region in Figure 4 of high metallicities. Practically without exception, they result from extrapolation beyond the largest model value of [M/H] = +0.5 exacerbated by large uncertainties in $\log S$,
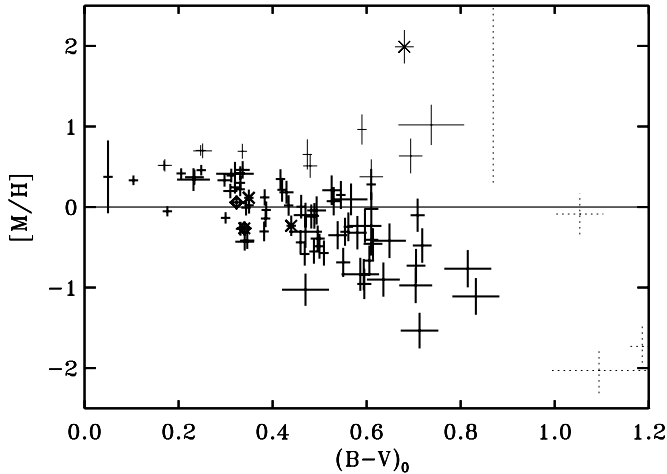
Figure 4. Determinations of [M/H] based on the measured BF strengths $\log S$. The horizontal error bars correspond to $\epsilon(B-V)$ while the vertical error bars combine all components of the $\log S$ error, as described in Appendix A.3, added in quadrature. The remaining symbols are as in Figure 3. Very large, positive values of [M/H] mainly result from linear extrapolation beyond the model atmosphere grid beyond [M/H] = +0.5 (see Figure 3); such extrapolated values are marked by thin symbols. Also uncertain are determinations for $(B-V)_0 > +0.85$ (thin dotted line symbols).

particularly at red colors. We were unable to determine metallicities for such binaries; this "saturation" effect happened for 12 binaries.

2. Because of the shape of the model function [M/H] = $F(B-V, \log S)$, metallicity determinations for red binaries with $(B-V)_0 > +0.85$ are entirely unreliable. Four such binaries were eliminated.

3. A trend of progressively lower metallicities for later spectral types extends over the whole range of colors. It starts at positive values of [M/H] for blue binaries and continues to negative metallicities for red binaries. The trend is most likely caused by the problems with pseudo-continuum placement discussed in Section 3 and summarized in Appendix A. We do not see such a color trend in results based on the Strömgren photometry m_1 index for a sub-sample of F-type systems (Section 6).

4. Early-type systems seem to show metallicities higher than solar. This may be due to the same systematic trend as above or it may result from the assumption of low, solar micro-turbulence value for our models: lateral pressure gradients in the outer layers may generate large turbulent velocities which may in turn lead to line strengths systematically larger than effective temperatures would imply.

In Table 5, the values of [M/H] for binaries suffering from the "saturation" are given in square parentheses; they are marked by thin symbols and error bars in the subsequent figures. Removal of such binaries may produce a bias in the final results against positive metallicities; this bias is one of the deficiencies of our analysis. We discuss determinations of [M/H] in full in Section 7 after a description of literature results on metallicities derived from Strömgren photometry.

6. STRÖMGREN PHOTOMETRY: THE LITERATURE DATA

It is not our intention to present a study of Strömgren photometry results because the literature data are available for only 35 EW binaries of our sample and because we feel that
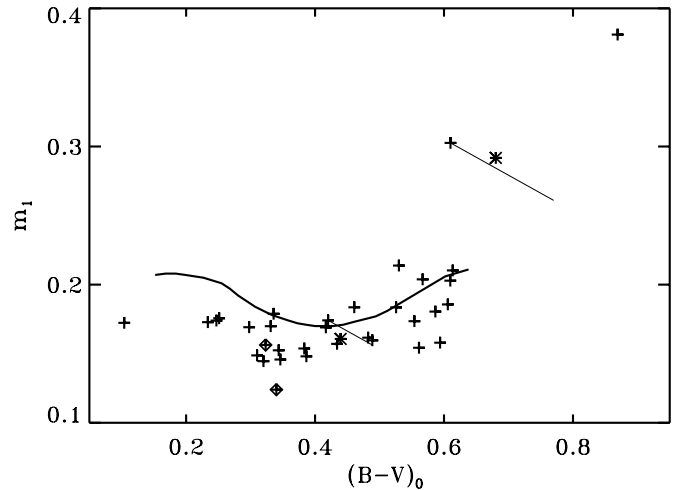

Figure 5. Reddening-corrected Strömgren indices m_1 from literature sources are shown by crosses vs. the de-reddened color $(B-V)_0$. The triple and detached binaries included in this study are marked by the same symbols as in previous figures. The reddening corrections are shown by lines for the cases when $E(B-V) > 0.05$. The line gives the Hyades standard relation for mid-A to early-G type dwarfs from Crawford & Perry (1966).

such a useful and relatively easy to conduct survey should be done with our results as an incentive.

The $m_1 = (v-b) - (b-y)$ index of the Strömgren photometry has previously been used to study the metallicity of W UMa-type binaries; we disregarded the index $c_1 = (u-v-(v-b)$ because of its sensitivity to gravity. Rucinski & Kaluzny (1981) obtained a few *uvby* observations per star and analyzed them together with similar fragmentary data from Hilditch & Hill (1975). They showed that the EW binaries appear to be Population I objects. Some systems were found to show elevated continuum levels in the u and v bands which could be assigned to chromospheric activity. Chromospheric emission would modify the m_1 index to mimic a decreased metal-line blanketing. A subsequent study of southern EWs (Rucinski 1983) showed that chromospheric emissions may be of concern only for the latest spectral types. Therefore, the UV excesses observed in some contact binaries are probably caused by genuine differences in metallicity, as originally suggested by Eggen (1967). The spread in metallicities derived from deviations in m_1 from the standard sequence (see below) within $-0.02 < m_1 < +0.08$ would correspond to metal abundances in the range $-0.6 < [M/H] < +0.4$.

Additional Strömgren photometry data for EW binaries could be found in random observations obtained within large-scale surveys of brightest stars and stars in clusters by Crawford & Barnes (1970), Blaauw et al. (1976), Schmidt (1976), Perry & Johnston (1982), Olsen (1983, 1993, 1994), and Jordi et al. (1996). So far, these data have not been analyzed in the EW metallicity context. The *uvby* data collected from the literature are listed in Table 6. The observations were of different quality and some entries in the table result from the averaging of several observations.

We estimated metallicity using the m_1 data corrected for interstellar reddening: $m_1 = m_1(\text{obs}) + 0.26 * E(B-V)$ (Strömgren 1966).[8] The values of the de-reddened m_1 are plotted in Figure 5 together with the standard relation for the Hyades defined by Crawford & Perry (1966). The figure shows that most binaries have lower metallicities than that of the Hyades, [M/H] = +0.13 (Pinnsonneault et al. 2004). Reddening

---

[8] The de-reddened index m_1 is sometimes called m_0.

Table 6
Strömgren *uvby* Photometry Literature Data

D1:D2	Name	$b - y$	m_1	c_1	Source
1:2	V417 Aql	0.421	0.146	0.360	1
1:6	FG Hya	0.385	0.182	0.333	1
2:1	AH Aur	0.401	0.195	0.423	1
2:3	DK Cyg	0.248	0.137	0.672	1
2:6	UZ Leo	0.242	0.143	0.685	1
2:8	V839 Oph	0.399	0.206	0.376	1
2:9	GR Vir	0.370	0.157	0.352	2
2:10	NN Vir	0.248	0.165	0.579	2
3:4	YY CrB	0.368	0.172	0.341	3
3:9	V753 Mon	0.213	0.152	0.704	2
3:10	OU Ser	0.405	0.152	0.293	3
4:5	EX Leo	0.331	0.153	0.395	2
4:8	V2377 Oph	0.407	0.172	0.322	2
5:4	DN Cam	0.216	0.163	0.631	2
5:8	V351 Peg	0.199	0.168	0.735	4
6:6	V972 Her	0.295	0.152	0.469	2
8:4	V921 Her	0.237	0.141	0.789	4
8:6	V1130 Tau	0.276	0.124	0.474	2
8:8	HX UMa	0.309	0.158	0.366	5
9:1	AB And	0.510	0.373	0.320	1
9:4	V2082 Cyg	0.224	0.166	0.698	2
9:10	V335 Peg	0.312	0.163	0.434	2
10:3	V449 Aur	0.086	0.163	1.019	6
10:5	SW Lac	0.471	0.284	0.268	1
11:3	TX Cnc	0.388	0.206	0.348	1
11:4	V1073 Cyg	0.281	0.170	0.666	1
11:6	AK Her	0.342	0.176	0.397	1
11:8	V566 Oph	0.305	0.142	0.445	2
11:10	AG Vir	0.156	0.166	0.824	1
12:1	OO Aql	0.464	0.261	0.291	1
12:5	AM Leo	0.356	0.177	0.341	1
12:7	V2612 Oph	0.382	0.149	0.361	7
12:9	W UMa	0.406	0.203	0.292	1
15:1	QX And	0.325	0.156	0.421	8
18:1	AW UMa	0.246	0.142	0.602	9, 10

References. (1) Rucinski & Kaluzny 1981; (2) Olsen 1983; (3) Olsen 1993; (4) Perry & Johnston 1982; (5) Blaauw et al. 1976; (6) Jordi et al. 1996; (7) Schmidt 1976; (8) Crawford & Barnes 1970; (9) Hauck & Mermilliod 1998; (10) Holmberg et al. 2009.

corrections may in some cases influence the m_1 indices quite strongly, as in the cases of OO Aql (12:1) and QX And (15:1) for which $E(B - V)$ is equal 0.16 and 0.07, respectively. As mentioned in Section 4.2, the case of OO Aql is a special one so we excluded this binary from further considerations. Metallicity estimates $[M/H]_m$ derived from the m_1 indices are described in Section 7.1.

7. RESULTS OF METALLICITY DETERMINATIONS

7.1. The Sub-sample of F-type Binaries

Discussion of metallicity determinations is facilitated when the sample is divided into three sub-samples, with the middle one consisting of the dominant F-type systems. There are 57 binaries in this sub-sample with spectral types within F1–G2 and colors within $0.32 < B - V < 0.62$; 52 of these binaries have well determined metallicities, i.e., not exceeding $[M/H] = +0.5$. Metallicities determined for the red and the blue sub-samples could not be related to the m_1-based results and are not discussed in the following. The reason that as many as almost two-thirds of the sample are F-type EW binaries is a combination of the
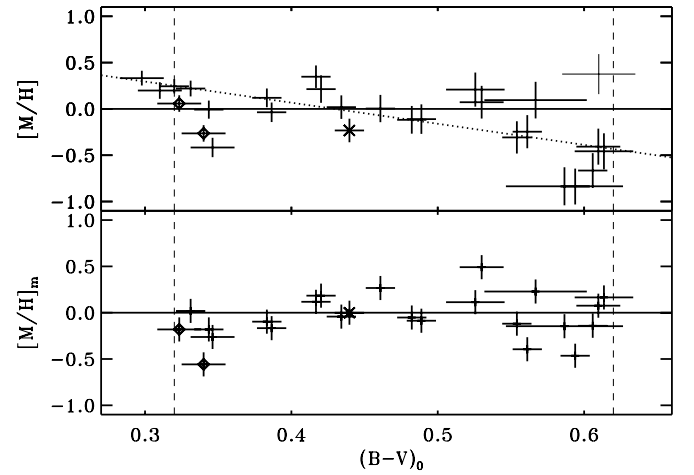

Figure 6. Comparison of our spectroscopic metallicity results [M/H] (upper panel) with metallicities $[M/H]_m$ estimated from the m_1 index, as described in the text (lower panel). The dotted line in the upper panel gives the linear fit to the differences between the BF-based and m_1-based determinations for 24 F-type binaries within $0.32 < (B - V)_0 < 0.62$. OO Aql (12:1) at the right end was not used in the fit (see the text); it is marked by a thin symbol.
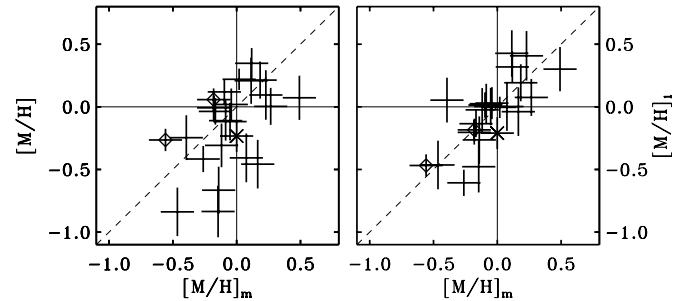

Figure 7. Correlations of the BF-based metallicities with the m_1-based ($[M/H]_m$) metallicities for the EW binaries of the "F-type sub-sample" ($0.32 < (B - V)_0 < 0.62$). The vertical axes of both panels show [M/H] and the trend-corrected $[M/H]_1$ (see Section 7.2), respectively.

relatively shallow depth of the DDO survey and of the shape of the luminosity function for the solar-neighborhood stars.

Metallicities for the F-type sub-sample of the EW binaries were derived using the calibration of Crawford & Perry (1976), $[M/H]_m = [M/H]^{\text{Hyades}} - 13 \times \delta m_1$, with $\delta m_1 = m_1^{\text{Hyades}} - m_1$, using the updated metallicity of Hyades, $[M/H]^{\text{Hyades}} = +0.13$ (Pinnsonneault et al. 2004). This calibration cannot be used for stars with $(B - V)_0 < 0.32$ because then a c_1-index dependent term should be included. c_1 is particularly sensitive to gravity, a dependence which we disregarded, and can be more affected by ultraviolet chromospheric emission than m_1. Because of the inhomogeneity of the literature *uvby* data, we did not use any observational errors and uniformly set the same error for the m_1-derived metallicities, $\epsilon[M/H]_m = 0.13$. This number is approximate and assumes that the typical error of m_1 is 0.01, and results from the accumulation of observational, reddening correction and Hyades-sequence subtraction errors. The comparison of the BF-based and m_1-based [M/H] determinations is shown in Figure 6 for 24 binaries which have determinations utilizing both methods.

Figure 6 shows a color trend in the BF-based values of [M/H]. This is the same trend as in Figure 4 (Section 5.3), but within a shorter color range. No such trend is obvious in the m_1-based values $[M/H]_m$. The values of [M/H] and $[M/H]_m$ correlate rather weakly, as is visible in the left panel of Figure 7. The
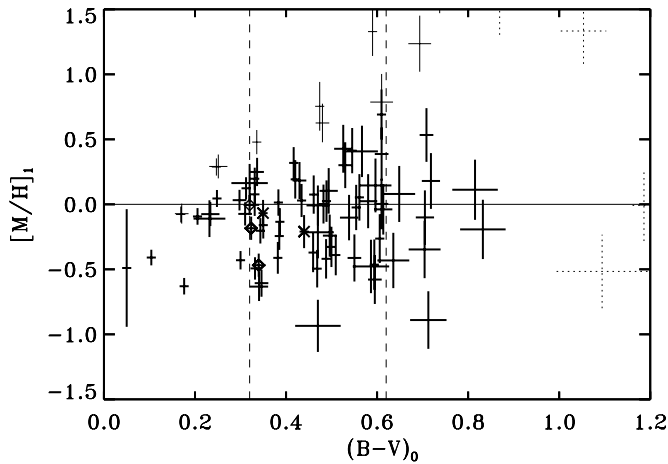
Figure 8. Metallicities $[M/H]_1$ obtained from the BF-based values of $[M/H]$, after the correction for the trend determined within the color range $0.32 < (B-V)_0 < 0.62$, as in Figure 6. The values of $[M/H]_1$ are explicitly tied to the m_1-based system. The thin symbols are for EW systems for which the BF line strengths could not provide reliable metallicity estimates; these data points are shown for illustration only and have not been used in our discussion of the EW metallicities.

Pearson correlation coefficient is $C_P = 0.48 \pm 0.03$, while the Spearman rank coefficient is $C_S = 0.53 \pm 0.01$. The positive correlation indicates that the deviations from zero metallicity are most probably real, but the significance of the correlation is low. We stress that the two methods are entirely independent.

7.2. Correction for the Color Trend

We decided to remove the color trend in the determinations of $[M/H]$ by fitting and subtracting a linear color dependence based on 24 binaries of the F-type sub-sample which have reliable metallicities derived using spectroscopic and photometric methods. We had a choice here: (1) the fit could be fully independent of the m_1-derived results, or (2) we could directly relate the BF-based results to the Strömgren photometry results by fitting the individual differences. We decided to follow the latter route and fitted a linear $(B-V)_0$ dependence to the differences, $[M/H]_{trend} = [M/H] - [M/H]_m$. Subtraction of such a relation brings the BF-derived data into the system established by the m_1 index preserving information on metallicities of individual objects. The trend is given by: $[M/H]_{trend} = (-0.05 \pm 0.04) - (2.28 \pm 0.40) \times [(B-V)_0 - 0.45]$. The standard deviation for a single difference (after allowing for two degrees of freedom) is 0.19 which gives independent information on the combined uncertainties of both methods of the metallicity determination. To add up quadratically to 0.19, with the assumed error $\epsilon[M/H]_m = 0.13$, the error of the BF-based determinations would have to be $\epsilon[M/H]_1 \simeq 0.14$. This is consistent with the median (0.16) of individual errors derived through propagation of individual uncertainty contributions (see Appendix A.3 and Table 5).

The values of $[M/H]_1 = [M/H] - [M/H]_{trend}$ show a tighter correlation with the m_1-based results than the uncorrected metallicities $[M/H]$, with the respective correlation coefficients, $C_P = 0.74 \pm 0.02$ and $C_S = 0.73 \pm 0.01$ (see the previous section). The correlation is shown in the right panel of Figure 7. We list the values of $[M/H]_1$ in Table 5 and show them versus $(B-V)_0$ in Figure 8. They may be considered to be the final results of this analysis in the sense that they should correctly reflect differences in individual metallicities among stars. While we determined them for all binaries of this study extending the
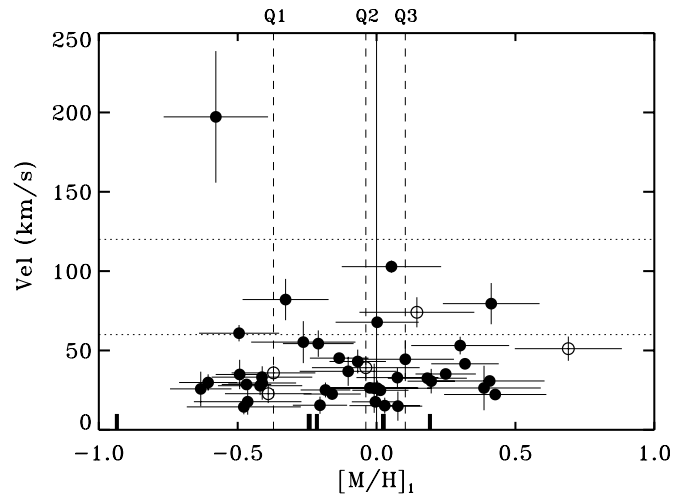

Figure 9. Relation between the metallicity index $[M/H]_1$ and the total spatial velocity for F-type stars (filled circles), as described in Section 8. Velocity data taken from Bilir et al. (2005) are marked by open circles. The high-velocity binary FU Dra is the single point in the upper left of the figure. The 60 and 120 km s^{-1} lines delineate (arbitrary) velocity ranges to distinguish stars of small, moderate and large spatial velocities. Binaries without spatial velocities are marked by thick ticks along the lower horizontal axis. The quartiles of the distribution of $[M/H]_1$ for 52 F-type binaries are marked along the upper horizontal axis and shown by vertical broken lines.

trend to all colors, they are strictly meaningful for the F-type sub-sample and for values $[M/H]_1$ which were obtained without extrapolation beyond the model grid with $[M/H] > +0.5$.

It is useful to compare Figure 8 with Figure 4. The data points apparently follow the horizontal line corresponding to the solar value. We stress that, in terms of the zero point, the values of $[M/H]_1$ are entirely dependent on the m_1 calibration of Crawford & Perry (1976) for the F-type sub-sample. In addition, removal of the trend makes the results for the few early-type ($(B-V)_0 < 0.25$) binaries ambiguous: the metallicities as determined initially, i.e., $[M/H]$, were mostly positive, but after the trend has been removed, they are now negative in $[M/H]_1$. Possibly, the trend correction should not extend into the domain of early-type EW binaries: the continuum placement problems are practically absent for these stars while the integrated line strengths $\log S$ are well defined and not very small, typically at about $1/2$ strength of that for the template (see Figure 3). We simply cannot state anything firm about metallicities of the early-type binaries. Even less trustworthy are metallicity determinations for stars with spectral types later than G2.

7.3. Metallicities of the F-type Sub-sample Binaries

The correlation observed for the F-type sub-sample between the trend-corrected metallicities $[M/H]_1$ and the m_1-based metallicities $[M/H]_m$ indicates that *both* techniques provide meaningful results. Thus, it strongly supports the view that Strömgren photometry δm_1 deviations are indeed due to metallicity differences and that they are not affected by chromospheric activity. While the inter-comparison of the BF-based and m_1-based results and determination of the color trend utilized 24 binaries in common, there are more than twice as many F-type binaries (52) with well determined spectroscopic metallicities $[M/H]_1$. This number is, however, still too small for a statistical analysis. The distribution of the trend-corrected metallicities $[M/H]_1$ is shown in Figure 9.

The $[M/H]_1$ distribution for all 52 F-type binaries extends within $-0.65 < [M/H]_1 < +0.5$, but the width is partly affected

by the large determination errors (the median $\epsilon[M/H] = 0.16$, see Appendix A). To reduce their influence, the distribution has been characterized by low-order moments: the $mean([M/H]_1) = -0.10$, the dispersion $\sigma[M/H]_1 = 0.33$, and the mean absolute deviation $\delta[M/H]_1 = 0.26$. The distribution is asymmetric with a tail toward low metallicities: the lower quartile is $Q_1([M/H]_1) = -0.37$, the median $Q_2([M/H]_1) = -0.04$ and the upper quartile $Q_3([M/H]_1) = +0.10$. If we disregard the asymmetry and assume that the observational errors broaden the $[M/H]_1$ distribution by 0.16 (the median of all individual, propagated errors), then—formally—the full dispersion of $[M/H]_1$ is reduced to 0.29. Thus, in the simplest terms, the distribution can be characterized as $\overline{[M/H]_1} = -0.1 \pm 0.3$. Keeping in mind that our result is entirely dependent on the adjustment to the m_1-based metallicity scale, the small value of the mean metallicity and their relatively narrow observed range for the F-type sub-sample of the EW binaries is consistent with typical metallicities in the solar neighborhood where the age range from the present to 10 Gyr corresponds to metallicities ranging from +0.15 to −0.3 (Reid et al. 2007).

The binaries with $[M/H]_1$ outside the $Q1–Q3$ quartile range by 0.1, that is outside $[-0.47, +0.20]$, are listed below. The pairs of numbers in the square brackets give $[M/H]_m$ and $[M/H]_1$; their differences can be used to appreciate the level of uncertainties in the metallicity determinations.

Large metallicity, $[M/H] > +0.20$.
V839 Oph (2:8) [+0.49, +0.30],
V2377 Oph (4:8) [+0.11, +0.43],
V335 Peg (9:10) [+0.12, +0.32],
W UMa (12:9) [+0.23, +0.41].

Low metallicity, $[M/H] < -0.47$.
DK Cyg (2:3) [−0.26, −0.61],
V1130 Tau (8:6)[−0.56, −0.47] (detached binary),
AM Leo (12:5) [−0.15, −0.48].

As mentioned before, only about one-half (24) of all F-type binaries with reliable metallicity determinations (52) have Strömgren photometry data. Among the binaries with only spectroscopic metallicities, we note several low-metallicity outliers with $[M/H]_1 < -0.47$: XZ Leo (2:7), FU Dra (3:5), GM Dra (6:5), FP Boo (10:4) and V1003 Her (13:2) with $[M/H]_1 = -0.63, -0.58, -0.50, -0.49$ and −0.93. Among these stars, FU Dra is a high-velocity star ($V_{tot} = 197$ km s^{-1}), apparently the only such one in the analyzed sample (Section 8).

8. KINEMATIC PROPERTIES OF EW BINARIES

Space velocity is the only other independent observable quantity which depends on stellar age. In this section we describe an attempt to correlate metallicities with the spatial velocities of the EW binaries. One expects that most of the binaries belong to the disk population which dominates in the solar neighborhood. The oldest, highest-velocity, lowest-metallicity, halo or Population II stars are very rare, with a relative frequency of only 0.1% (Weistrop 1972; de Jong et al. 2010). Within the disk population, most of the stars, about 93% (de Jong et al. 2010) to 96% (Aumer & Binney 2009), are *thin-disk* objects (scale-height <300 pc) with metallicities similar to the solar metallicity. According to Schönrich & Binney (2009), all thin-disk stars may be younger than 7 Gyr. The *thick-disk* population stars (Gilmore & Reid 1983) appear in the solar neighborhood with a relative frequency of the remaining few percent; this number is the subject of intensive research.

They have distinctly lower metallicities than the solar, typically $[M/H] \simeq -0.5$ to -1.0, but with a wide range extending down to metallicities as low as −2.2, i.e., including objects formerly known as "intermediate Population II" or "47 Tuc population" with ages >10 Gyr. Velocities of disk population stars are well organized and reflect the global galactic rotation. Their dispersions increase over time (Wielen 1977) through dynamical processes such as scattering by molecular clouds and spiral arms and processes following accretion of low-luminosity satellites by the Galaxy. Thus, space velocities can be used statistically as an age indicator for a group of objects. Allowance must be made for the spectral-type dependence because velocity dispersions increase for late-type stars (Seabroke & Gilmore 2007; Aumer & Binney 2009; Holmberg et al. 2009) as a result of longer survival times for lower stellar masses.

After the pioneering investigation by Guinan & Bradstreet (1988), the only study of kinematic properties of the EW binary stars was by Bilir et al. (2005) who considered all short-period binaries including the EW systems. It utilized results on the center-of-mass velocities, V_0, obtained during the DDO program as published in the papers DDO-1 to DDO-9, so that results from the six subsequent DDO papers (Table 1) were not included; instead the study used older, inhomogeneous data from various sources. In this paper we purposefully avoid diversity of sources and determine space velocities only for the EW binaries which have proper motions based on the new *Hipparcos* reductions (van Leeuwen 2007)[9] and the center-of-mass radial velocities V_0 determined during the entire DDO survey. The input data are listed in Table 7.

The calculated U, V, W space velocity components, as listed in Table 8, are corrected for the solar motion (Coskonoglu et al. 2011) relative to the local standard of rest (LSR), with U counted positive toward the Galactic center, i.e., using the same convention as Bilir et al. (2005). We found that median differences between that paper and our determinations reflect only the difference in the treatment of the LSR correction. We brought the Bilir et al. velocities to the LSR-corrected system of velocities by adding the solar velocity correction, [+8.5, +13.4, +6.5] km s^{-1} as determined by Coskonoglu et al. (2011). After the adjustment, the median values for the common stars differed by only [−1.6, +0.4, −0.3] km s^{-1} which mostly reflected the different assumed distances to the binaries. The median error for our determinations of velocity components is 1.9 km s^{-1}, which is identical to that in Bilir et al. However, individual velocities sometimes differ quite a lot and our error estimates generally tend to be larger. The largest differences appeared for FG Hya (1:6), $U = +70.1$ km s^{-1} for Bilir et al. and $U = 41.9$ km s^{-1} in our case, and for V2357 Oph (8:5), $[V, W] = [-56.8, -37.0]$ km s^{-1} for Bilir et al. and $[V, W] = [-93.7, -57.7]$ km s^{-1} for our determinations. These large discrepancies result from two sources: (1) our use of exclusively van Leeuwen (2007) proper motions with re-determined errors, and (2) larger uncertainties in our assumed distances, which are hopefully more realistic. Thus, we used mostly our velocities, but—when not available because of the more restrictive criteria in the reductions of van Leeuwen (2007)—we added Bilir et al. determinations. The latter are listed in Table 8 in square brackets. The number of new velocity determinations is 65 with an additional 13 velocities from the

---

[9] The important, extreme short-period, red binary CC Comae (which had not been observed by *Hipparcos*) was included using the data of Klemola (1977). Its kinematic properties are similar to those of the F-sub-sample stars.

Table 7
Kinematic Input Data

D1:D2	Name	HIP	V_0 (km s^{-1})	μR.A. (mas yr^{-1})	μDecl. (mas yr^{-1})
1:2	V417 Aql	96349	-14.20 ± 1.40	-2.24 ± 2.76	-24.70 ± 1.63
1:6	FG Hya	41437	-5.70 ± 1.20	5.06 ± 1.95	-63.72 ± 1.56
1:9	BB Peg	110493	-28.90 ± 1.40	20.00 ± 2.42	-25.56 ± 1.68
1:10	AQ Psc	6307	-12.90 ± 0.40	-8.93 ± 1.08	14.25 ± 0.73
2:1	AH Aur	30618	31.95 ± 1.45	15.23 ± 2.72	-12.50 ± 1.64
2:2	CK Boo	71319	37.04 ± 0.75	71.05 ± 1.05	-87.41 ± 1.08
2:3	DK Cyg	106574	-5.53 ± 1.48	-28.27 ± 0.91	-19.24 ± 1.14
2:6	UZ Leo	52249	-8.18 ± 1.12	-21.35 ± 1.25	-1.88 ± 0.75
2:7	XZ Leo	49204	-2.03 ± 1.43	-16.49 ± 1.95	3.00 ± 1.01
2:8	V839 Oph	88946	-63.81 ± 1.09	-34.53 ± 1.68	2.82 ± 1.54

Notes. Additional column headings not explained in the previous tables: HIP: the *Hipparcos* mission number (HD numbers and other names are given in the respective DDO papers); V_0: center-of-mass radial velocity from the DDO survey. Proper motions μR.A. and μDecl. have been taken from the new reductions of the *Hipparcos* data by van Leeuwen (2007).

(This table is available in its entirety in machine-readable and Virtual Observatory (VO) forms in the online journal. A portion is shown here for guidance regarding its form and content.)

Table 8
Space Velocity Components

D1:D2	Name	U (km s^{-1})	V (km s^{-1})	W (km s^{-1})
1:1	GZ And	[14.0 ± 1.9]	[21.1 ± 1.9]	[2.4 ± 2.0]
1:2	V417 Aql	12.2 ± 4.4	−12.8 ± 4.6	−0.9 ± 5.1
1:5	V829 Her	[5.6 ± 1.0]	[−0.5 ± 1.0]	[0.8 ± 1.1]
1:6	FG Hya	41.9 ± 6.6	−31.2 ± 10.0	−18.0 ± 5.6
1:9	BB Peg	0.7 ± 6.1	−34.8 ± 6.1	−14.7 ± 8.9
1:10	AQ Psc	14.6 ± 1.4	19.0 ± 2.1	22.0 ± 1.2
2:1	AH Aur	−21.7 ± 2.9	1.2 ± 2.7	14.7 ± 2.8
2:2	CK Boo	81.8 ± 11.0	2.9 ± 2.5	6.6 ± 6.5
2:3	DK Cyg	27.0 ± 4.0	6.5 ± 2.9	10.8 ± 1.5
2:5	V842 Her	[−25.3 ± 3.4]	[−33.9 ± 2.0]	[−23.7 ± 2.3]

Notes. The table lists new space velocity determinations except for velocities from Bilir et al. (2005) which are given in square brackets (after the LSR correction, as described in the text). The remaining columns have column headings as in other tables.

(This table is available in its entirety in machine-readable and Virtual Observatory (VO) forms in the online journal. A portion is shown here for guidance regarding its form and content.)
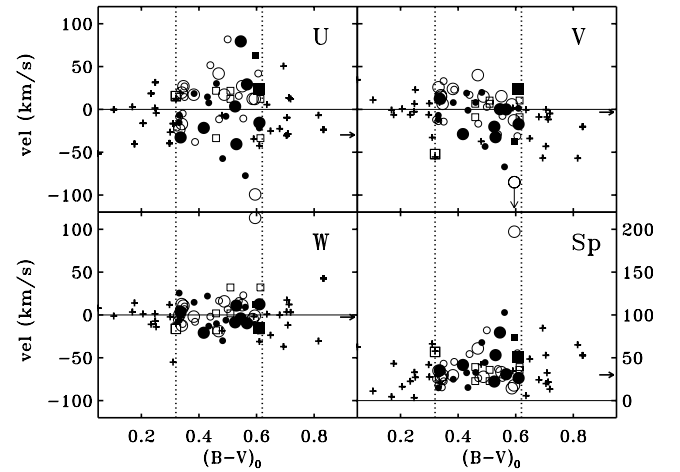

Figure 10. UVW components of galactic velocities of the EW binaries discussed in this paper (the three upper and left panels) and the total spatial velocities (the lower, right panel). Metallicities [M/H]$_1$ for the F-type binaries with $0.32 < (B - V)_0 < 0.62$ are coded by the size of the symbols: they are small for $-0.4 < $ [M/H]$_1 < +0.2$ and large outside this range. The positive metallicities ([M/H]$_1 > 0$) are shown by filled symbols and negative metallicities ([M/H]$_1 \leqslant 0$) are shown by open symbols. Square symbols are used for binaries with velocities taken from Bilir et al. (2005). Velocities for binaries without reliable [M/H]$_1$ are marked by crosses. Velocities for the red, short-period binary CC Com (12:2) are marked by the right-directed arrows. For the high-velocity binary FU Dra (3:5), the velocity component $V = -119.4$ km s^{-1} is outside the coordinate box.

Bilir et al.; among those 78, 50 binaries belong to the F-type sub-sample.

Figure 10 shows that space velocities of EW binaries are rather typical for the solar neighborhood. We discuss the results in terms of the velocity dispersions below. Here we note that only one binary has a large velocity: for FU Dra (3:5) the space velocity vector is $[-99.3, -127.2, +113.4]$ km s^{-1}, but the errors are large, about ± 25 km s^{-1} for each component. The full space velocity of the star is 197 km s^{-1}, which sets the binary apart from the rest of our sample. Our determination gives a low metallicity of FU Dra, [M/H]$_1 = -0.58 \pm 0.19$, but there exists no Strömgren photometry to support this value. This binary may be the only *thick-disk* representative in our sample.

Besides FU Dra, there are six other F-type stars with velocities $V_{\rm space} > 60$ km s^{-1} (see Figure 9): CK Boo (2:2): [82, −, −0.33], GR Vir (2:9): [68, −0.05, 0.00], OU Ser (3:10): [103, −0.39, +0.05], GM Dra (6:5): [61, −, −0.50], and HN UMa (8:8): [80, −, +0.41], where the first number after the star's identification is the spatial velocity in km s^{-1} while the second and third numbers are [M/H]$_m$ and [M/H]$_1$. These binaries may show

some tendency for negative metallicities, but the data are not accurate enough for such a conclusion.

The scatter of velocities as shown in Figure 10 gives us some indication of the typical age of the EW sample. The velocities increase for later spectral types within the F-type sub-sample which is typical for the solar neighborhood. The formal dispersions of velocity components for 43 F-type binaries (excluding FU Dra) are: $\sigma U = 32.2$ km s^{-1}, $\sigma V = 22.6$ km s^{-1} and $\sigma W = 13.1$ km s^{-1}. When the sample is enlarged to 49 objects by adding slightly less secure velocities from Bilir et al. (2005), the dispersions are: $\sigma U = 32.7$ km s^{-1}, $\sigma V = 22.7$ km s^{-1} and $\sigma W = 14.4$ km s^{-1}. When compared with the results of Holmberg et al. (2009), the velocity dispersions suggest the *thin-disk* population with the age of about 3.0–5.5 Gyr.
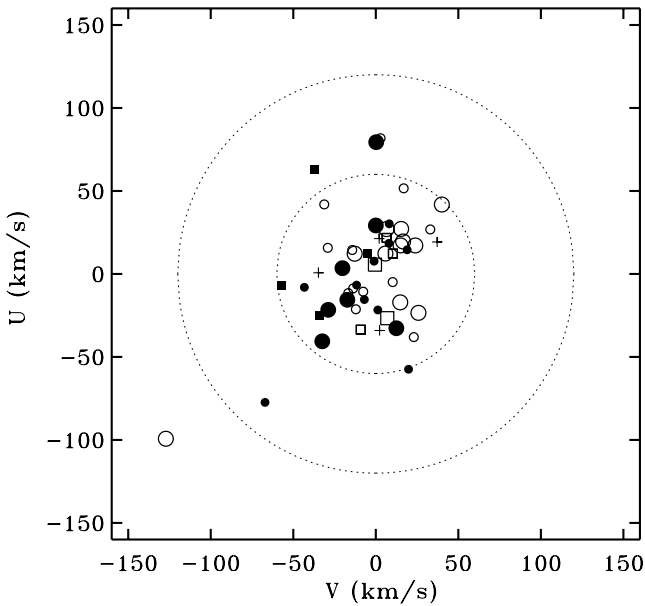
Figure 11. Galactic disk-plane components of the space velocity, U and V, for the F-type sub-sample are shown here with metallicities coded by the size of the symbols: small for $-0.4 < [M/H]_1 < +0.1$ and large outside this range, with positive metallicities shown by filled symbols and negative metallicities shown by open symbols. Squares are for binaries with velocities taken from Bilir et al. (2005). Crosses mark binaries with available velocities but without determined metallicities. The dotted line circles have radii of 60 and 120 km s^{-1}. This figure can be directly compared with Figure 2 in Guinan & Bradstreet (1988).

The galactic-plane velocity components U and V for the F-type sub-sample are shown in Figure 11. The low- and high-metallicity objects do not separate strongly in the two velocity components; only FU Dra is set apart from the rest of the EW binaries. The absence of an obvious correlation between space velocities and metallicities can be also seen in Figure 9.

The special position of FU Dra is particularly strongly visible in the W-component velocities (the lower left panel of Figure 10) and in their histogram (Figure 12). The W velocity dispersion is an useful indicator of the population: for the solar neighborhood, the characteristic values are $\sigma W \simeq 20$ km s^{-1} for the thin disk and 45 km s^{-1} for the thick disk (Edvardsson et al. 1993; Veltz et al. 2008). Thus, the small scatter in the W velocities in Figure 12 is indicative of small velocity errors, reliable distances, and strongly suggests that the analyzed EW binaries belong to the thin-disk population.

9. METALLICITIES AND EVOLUTION

The prevailing view on how EW binaries form and evolve sees them as a result of the angular-momentum-loss driven evolution of close but detached binaries. The original periods of these binaries are expected to be about 2.5–3.5 days; they are rather mildly evolved objects when they enter into mass-exchange and/or mass-loss phase. It is not clear if during the contact-binary formation the mass ratio reverses, but many indications and theoretical predictions suggest this to be the case (Stepien 2006, 2009). An event of mass-reversal would expose the interior of the mass-losing companion, but we would not see any changes in our spectral window. Besides, most of the binary components are not sufficiently massive for the CNO cycle and an interruption of the p–p cycle and exposure of the interior material will not alter the observable metallicities. Therefore, the metallicities that we measured reflect properties of EW progenitors and are not expected to be modified by their subsequent evolution.
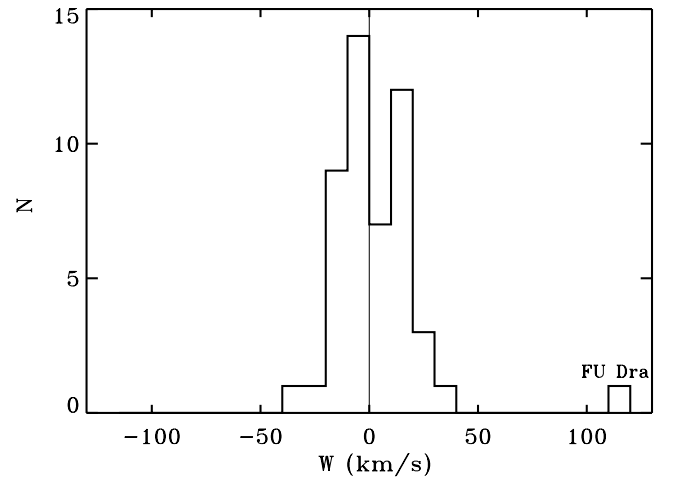

Figure 12. Histogram of W velocity components (perpendicular to the galactic disk) for the F-type binaries. OO Aql has been excluded from the sample.

The evolutionary state of a EW binary requires some assumptions on the energy-exchange and mass-exchange model. While the Lucy model (Lucy 1968a, 1968b) is the most popular model for EW binaries, it must still be the subject of continuing scrutiny: it provides excellent reproduction of light curves (which however have low information content) but the spectroscopic support is still rather fragmentary. The strict agreement with the Lucy model has been recently questioned for the particularly important and well-studied low mass-ratio binary AW UMa (Pribulla & Rucinski 2008). On the other hand, very strong interaction between the components cannot be questioned because we do see an excellent equalization of temperatures over the whole binary structure. Irrespective of the detailed model, much can be said about the state of these binaries by simply using the essential observational quantities: (1) the period, P, which is known practically without any error, (2) the mass ratio, $q = M_2/M_1 \leqslant 1$, known from RV determinations with uncertainties typically at the level of $\epsilon q \leqslant 0.01$, and (3) the $(B - V)_0$ color which is the least reliably known, but a crucial quantity, as it can be used to relate the above two quantities to the thermal state of the stars. To this set, we can now add two quantities which correlate with the age, the metallicity $[M/H]_1$ and the space velocity vector $[U, V, W]$.[10]

The period–color relation in Figure 13 summarizes the essential properties of the EW binaries discussed in this paper in terms of periods, colors and metallicities. The relation was discovered by Eggen (1961, 1967) and has been used since as one of the tools to infer the evolutionary state of EW binaries. Its existence has been the strongest argument for inferring that the EW binaries generally follow the main sequence with the color being a useful proxy for the mass of the primary component. The $[M/H]_1$ metallicity determinations of the F-type sub-sample (between the two dotted horizontal lines) are coded in Figure 13 by open and filled circles of different size. The broken line in the figure gives the "short-period blue envelope" (SPBE) as defined in Rucinski (1998b). Stars close to the SPBE are expected to be either (1) un-evolved, without any evolutionary expansion, or (2) of low metallicity, because of the smaller sizes of such binaries and the reduced metal blanketing in the B-band (Rucinski 2000). We know that the EW binaries cannot be young and un-evolved because they do not appear in young

---

[10] We avoid using individual masses obtained from radial velocity semi-amplitudes K_i because they are geometric-model dependent through the orbital inclination.
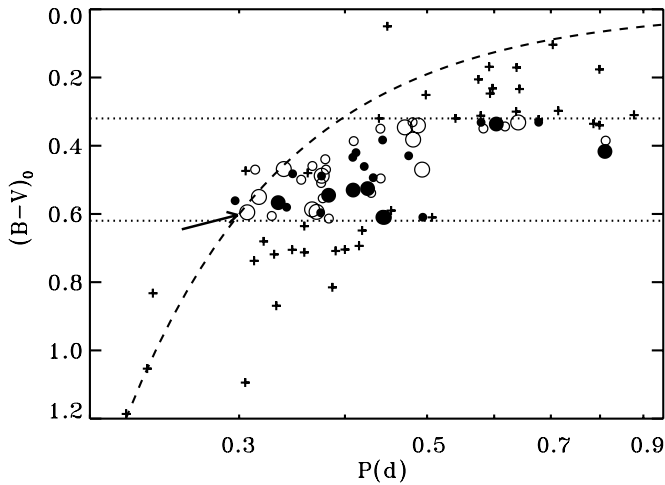
Figure 13. Period–color relation for the EW binaries analyzed in this paper with metallicities $[M/H]_1$ coded by circles for the F-type sub-sample: the sizes of the circles are small for $-0.4 < [M/H]_1 < +0.2$ and large outside this range, with positive metallicities shown by filled symbols and negative metallicities shown by open symbols. The stars not in the F-sub-sample or with unreliable determinations of metallicities are marked by crosses. The two detached binaries have been removed from this plot which applies to contact binaries only. The figure uses the same convention as in the papers of Eggen (1961, 1967) with the color axis directed downward and with the logarithmic scale for the period. FU Dra is pointed out with an arrow. The broken line gives the "short-period blue envelope," as discussed in the text.

Figure 14. Spectroscopic mass ratios q vs. orbital period P (in days). The F sub-sample binaries with reliable determinations of $[M/H]_1$ are marked by circles with small sizes for $-0.4 < [M/H]_1 < +0.2$ and large outside this range, with positive metallicities shown by filled symbols and negative metallicities shown by open symbols. Binaries with spatial velocities >60 km s^{-1} are marked by slanted bars and FU Dra is additionally pointed out with an arrow. The stars outside the F-sub-sample range and with unreliable determinations of metallicities are marked by crosses. The two detached binaries in the upper right corner are marked by rhombuses while the unique contact-binary OO Aql is marked by a triangle.

clusters, so the low-metallicity assumption for systems close to the SPBE is more likely. We see in Figure 13 that the metal-poor binaries show some tendency to be closer to the SPBE than those with high metallicities. The high-velocity, low-metallicity binary FU Dra is exactly on the SPBE line. In general, however, the separation in metallicities is not very strongly visible in this figure.

Figure 14 shows the relation between the orbital period and the spectroscopic mass ratio. This relation has already been shown before (Rucinski 2010a, 2010b) to demonstrate an unexpected bifurcation in the mass ratio of contact binaries observed in the DDO survey: for periods longer than $P \simeq 0.35$ days, the mass ratio can be either small, $q < 0.5$, and decreasing with the period, or large, $q > 0.7$. There is a prominent gap between the two branches. The DDO survey was not biased in any way against the mass ratio so that this result is well established.

The upper branch in Figure 14 is defined by atypical binaries: the two detached binaries (V753 Mon and V1130 Tau) appear there as expected, but among genuine EW binaries we see only those with the earliest or the latest spectral types. The early-type ones are V2150 Cyg (4:3) and V449 Aur (10:3) with the spectral types estimated as A5/6V and A5/6V (or A2IV). The late-type are EW binaries with peculiarities: two binaries with masses typical for the F spectral type ($>2\,M_\odot$) yet with late spectral types, SW Lac (10:5) and OO Aql (12:1) (the latter additionally with highly uncertain reddening, see Section 4.2) and AU Ser (14:9) showing a very large, single, dark spot.[11]

The better populated, lower branch in Figure 14 appears to contain genuine contact binaries. Gazeas & Niarchos (2006) pointed out that the less massive components of binaries located along this branch have very similar masses of about $0.5\,M_\odot$. The lower branch contains several F-type binaries with reliable determinations of metallicities $[M/H]_1$. Of special note are the shortest-period F-type binaries with orbital periods around $P \simeq 0.3$–0.35 days, particularly a group with large spatial velocities and mostly low metallicities, hence probably older than the rest. They all have small mass ratios, $q \simeq 0.1$–0.2. In contrast, the remaining F-type sub-sample binaries, presumably younger and/or less evolved, have larger mass ratios, $q \simeq 0.3$–0.6, and a wide range in metallicities. This mass-ratio spread at the shortest periods may be the best defined manifestation of evolution for EW binaries. Evolution toward small mass ratios was predicted from considerations of the stability of Lucy's model (Lucy 1968a, 1968b) in Lucy (1976). Although we see the predicted progression in the mass ratio (the vertical direction in Figure 14), we cannot exclude a systematic evolution to progressively shorter periods at a constant mass ratio.

No clear indication of evolution is provided by variations of orbital periods of EW binaries. The period variability is known to be strong and easily detectable (Kreiner 1977). In many cases it is relatively regular and induced by a companion as they are very common for EW binaries (Pribulla & Rucinski 2006; D'Angelo et al. 2006; Rucinski et al. 2007). However, it appears that the period variations must primarily reflect mass-transfer effects within the binary itself and not evolutionary effects. As shown in the study of period variations based on the Optical Gravitational Lensing Experiment survey (Kubiak et al. 2006), the period time derivative is equally likely be positive as negative and its size is typically large in the absolute sense, implying variations in time scales of about 1.5×10^6 yr. Such a rapid variability is simply too fast to result from evolutionary changes; it is at least some 10 times faster than the thermal time scale of the more massive component which is expected to determine the period evolution rate. These reasons, and the strong inhomogeneity of

---

[11] Large spots are easily detectable in BF profiles as well defined, migrating "notches," but they have not been detected in spite of extensive scrutiny of thousands of BF profiles for all EW binaries of the DDO program; AU Ser is an exception. Large spots which are invoked frequently to explain systematic discrepancies in photometric analyses of light curves may be an indication of a deficiency of the contact model (Pribulla et al. 2011). However, small, localized spots were seen in high-quality data for AE Phe (Barnes et al. 2004) and AW UMa (Pribulla & Rucinski 2008).
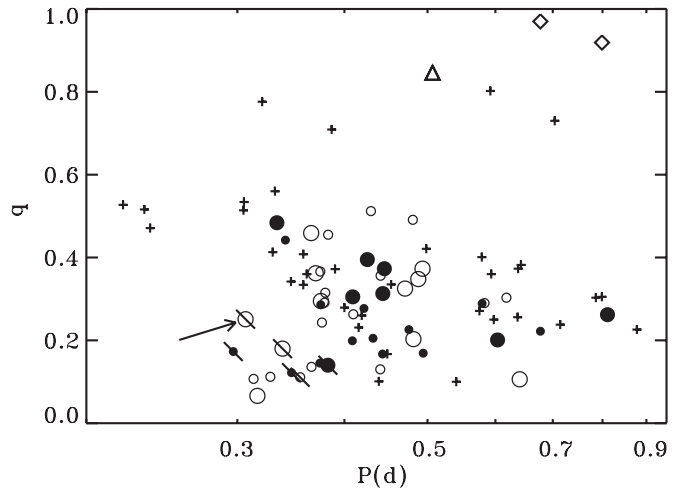
the period-variability data for our sample of 90 binaries, led us to regard the period changes as not related to their evolutionary state of the analyzed EW binaries.

10. DISCUSSION AND CONCLUSIONS

10.1. Summary of the Results

This paper presents a first attempt to determine the metallicities of W UMa-type systems from the spectroscopic data. A novel technique based on the BF method calibrated using the synthetic spectra was developed; it determines the integrated strengths of metallic lines within a set spectral window. Several implementation problems have been encountered; possible methods of circumventing them in the future are discussed in the next Section 10.2.

The most reliable metallicity determinations were obtained for the "F-type sub-sample" of early-F to early-G type systems with $0.32 < (B - V)_0 < 0.62$ consisting of more than one half of all binaries of the total sample of 90 objects. Our results are shown in the graphical form in Figure 3 (the raw determinations [M/H]) and in Figure 8 (the determinations corrected for a trend inherent to the method, $[M/H]_1$): the F-type EW binaries have roughly solar metallicities, but with a relatively large scatter which is partly due to the large determination errors. The spectroscopically determined metallicities, $[M/H]_1$, correlate with the Strömgren photometry m_1-based metallicities $[M/H]_m$ supporting the validity of both methods. The spectroscopic results strongly suggest that the m_1 index is a valid measure of metallicity and (for the F-type EW binaries) is not affected by chromospheric activity as was suspected before.

The distribution of $[M/H]_1$ for the F-type sub-sample extends between $-0.65 < [M/H]_1 < +0.5$ (Figure 9), with half of all systems having metallicities within $-0.37 < [M/H]_1 < +0.10$. The distribution is asymmetric, with the mean at -0.1, the median at -0.04 and a tail extending toward low metallicities. The determination errors are estimated at about $\epsilon[M/H] \simeq 0.16$ and they contribute to the width of the distribution. While the preferentially negative values of the metallicities is entirely consistent with a typical stellar population in the solar neighborhood, the distribution may be biased against positive metallicities. This is due to the line saturation effects and our removal of metallicities which required extrapolation beyond the largest model value of $[M/H] = +0.5$. It must be stressed that the absolute level (zero point) of our determinations is anchored to the m_1 calibration and is subject to any systematic error of the former.

We determined and analyzed the kinematic data for 50 binaries of the F-type sub-sample. We found that all but one (FU Dra) show small to moderate velocity dispersions in all three principal directions. The dispersion is particularly small in the direction perpendicular to the galactic disk, $\sigma W \simeq 14$ km s^{-1} which is a characteristic property of the solar-neighborhood, thin-disk population with a typical age of about 3.0–5.5 Gyr. The high-velocity binary FU Dra with $V_{tot} = 197$ km s^{-1}, $[M/H]_1 = -0.58 \pm 0.19$, shows $W = 113$ km s^{-1}. This may be the only thick-disk star in the sample or an object which experienced a strong out-of-plane scattering event in the past.

The findings concerning the F-type EW binaries lead to refinement of the conclusions of Guinan & Bradstreet (1988): while it is confirmed that the EW binaries are rather old objects, they do not seem to differ from most typical, thin-disk dwarfs in terms of their kinematic properties. The previous result used less accurate proper-motion data and included late-type EW binaries

which—similarly to other solar-neighborhood stars—tend to have larger velocities than F-type stars. With the exception of FU Dra which is moderately metal poor, we see no obvious correlation between metallicity and spatial velocity for 44 F-type sub-sample binaries with the new velocities and reliable determinations of $[M/H]_1$.

While the mean metallicities give almost no constraints on the ages, as the age–metallicity relation allows a range from the present to 10 Gyr (Reid et al. 2007), the ages estimated from the kinematics (3.0–5.5 Gyr) are in agreement with the upper limit for thin-disk stars not exceeding 7 Gyr as estimated from kinematic models (Schönrich & Binney 2009).[12] Because the EW binaries appear in large numbers in old open clusters, for example in NGC 6791 (Mochejska et al. 2002, 2005) with an age estimated at 7.7–9.0 Gyr (Grundahl et al. 2008), and in still much older globular clusters (Rucinski 2000), they must keep on forming during the lifetimes of these clusters. This explains the rising frequency of EW binaries with age for old open clusters (Kaluzny & Rucinski 1993; Rucinski 1998b) as having its source in the steeply increasing numbers of stars along the main sequence luminosity function rather than in the long survival times of the EW binaries.

The color (Figure 13) and the mass-ratio (Figure 14) dependences on the orbital period give interesting evidence on the evolutionary state of the analyzed EW binaries. Here, we see a group of binaries with relatively short periods ($0.3 < P < 0.4$ days) and low mass ratios ($0.05 < q < 0.3$) which have a tendency for large spatial velocities (>60 km s^{-1}) and low-metallicities. Thus, they appear to be old stars. Although we cannot say if these binaries evolved by drifting to small mass ratios (as predicted by Lucy's contact model) or to short orbital periods through loss of angular momentum, the special location of these binaries in Figure 14 is striking and requires further research.

Finally, we note that three triple systems with faint companions, $L_3/L_{12} < 0.05$, did not show drastic deviations from the other results, so very common triple systems with faint companions may be (cautiously) included in similar investigations. Also, the two equal-mass, detached binaries appeared to merge in between the genuine early-type contact binaries, but we could not contribute any firm results on their metallicities for these binaries because they fell outside of the best studied sub-sample of F-type binaries. The location of the detached binaries among the upper mass-ratio branch in Figure 14 may help in identifying pre-contact binaries or binaries masquerading to be in contact.

10.2. Recommendations for the Future

The spectroscopic metallicities were determined using the combined strengths of metallic lines within the spectral window 5080–5285 Å which contains the Mg I triplet. For early-F type EW binaries, for which our metallicity determinations are the most secure, the lines of the triplet produce about 10% of the total line strength within the window, so that mostly iron lines contributed to the measured line strength. However, the Mg I triplet contribution increases rapidly for later spectral types; with it, increases the dangers of contamination by chromospheric emission. Thus, the Mg I triplet window, which served well for RV determinations, is not the optimum region for line-strength measurements. Less congested spectral windows, such as the region of the Mg II 4481 Å line for spectral types B9V to A5V

---

[12] Feltzing & Bensby (2009) quote observational estimates on *a lower limit* to the thin-disk age of 9 Gyr. This issue appears to be far from being settled.

or the region around 6290 Å for late-type stars may give better results.

The pseudo-continuum placement was identified as the main limiting factor in our method. In the future, it will be essential to pay particular attention to the rectification step, perhaps by using nightly observations of smooth-continuum spectrophotometric standard stars or synthetic spectra calculated with and without the lines. When better temperature information for EW binaries becomes available (e.g., from infrared colors), an additional improvement could result from using model template spectra computed for individual binaries.

A systematic photometric survey of the W UMa-type binaries in the Strömgren *uvby* system is very much needed. Our spectroscopic results are in very good agreement with metallicities derived using the m_1 index data which require relatively lower observational expenditures than a spectral investigation. Finally, it would be interesting to repeat this work when new astrometric and spectroscopic data from the *Gaia* mission (Lindegren et al. 2008) and the *Gaia*-ESO Public Spectroscopic Survey (Gilmore et al. 2012) become available.

APPENDIX A

UNCERTAINTIES AND THE ERROR BUDGET

A.1. Pseudo-continuum and Rectification

Most EW binaries in the sample are cooler than the template HD 128167 (σ Boo, F2V, $B - V = 0.36$) so that the values of S are slightly larger than unity with the observed range $-0.2 < \log S < +0.5$. The measurements of S show a very small orbital-phase scatter. The median random measurement error computed from the orbital-phase scatter of $\log S$ is $\epsilon_1 = 0.0032$, with the smallest error in the sample of 0.0006 and the largest of 0.020. We describe below that these very small formal errors are not representative of the actual, much larger uncertainties.

The heavy velocity broadening and blending of late-type spectra caused by rapid rotation profoundly change their appearance, as can be seen in Figure 15. The figure illustrates a simpler case of rapidly rotating *single stars* at the $V \sin i$ values typically observed for components of EW binaries. One should note the strongly decreased depths and large depressions in the pseudo-continuum between the spectral lines. For EW binaries, the additional complication is the rapidly variable line blending
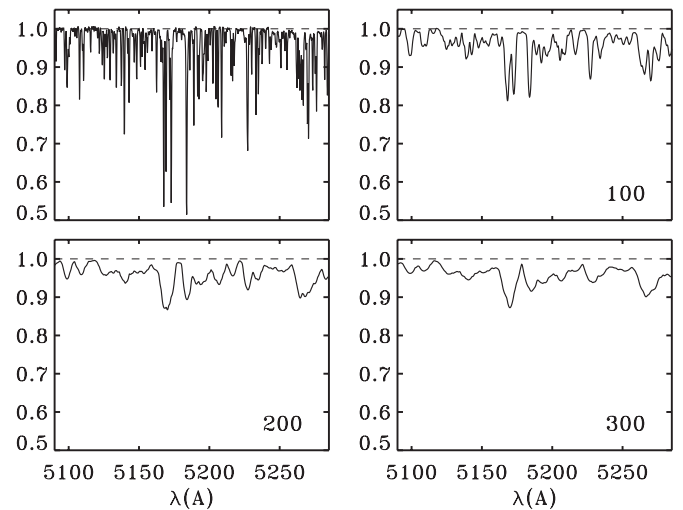

Figure 15. Broadening of the spectrum due to rotation. The upper left panel shows the template spectrum while the remaining panes give the template spectrum convolved with the theoretical rotational profiles of single stars for three values of $V \sin i$, 100, 200 and 300 km s^{-1}, as given in each of the panels. For the EW binaries the line broadening is complicated by additional phase-dependent blending.

in time scales as short as a few minutes. These rapid spectral variations have strong effects on observed pseudo-continuum levels with departures from the correct continuum level leading to changes in S. A downward displacement by Δ (see Figure 1) from the real continuum level to a pseudo-continuum level will cut off weak lines and will reduce S by the factor $(1 - \Delta)$.

For an idealized case of a uniform (across the spectral window) vertical shift and the spectrally matching template, the BF technique has the potential to permit evaluation of Δ from the BF baseline displacement, δ: when $\delta = 0$, the spectral continuum is correctly positioned; for any $\delta \neq 0$, the integral of the BF above the baseline requires linear scaling by $1 + \Delta$ with $\Delta = C \times \delta$, with C being a factor converting linear units of the spectrum height into the units of the S integral. Unfortunately, such an approach could not be used here because of uncertainties at the rectification step of the spectral processing due to absence of information on location of the actual continuum level. Rectification hides—in its simplicity—many complex factors. For lack of real information, it is usually done by joining the highest points of the pseudo-continuum. This not only corrects for the genuine depression of the stellar continuum due to the line blending, but mainly removes many instrumental problems affecting the spectra, such as chromatic efficiency variations in the spectrograph (the grating efficiency combined with the detector sensitivity non-uniformities), positioning of the object on the spectrograph slit, chromatic differential refraction, etc. These contributions are not uniform across the spectral window. Thus, $\delta = 0$ is not a guarantee that the proper level of the spectral continuum has been established.

Uncertainties in the rectification did not substantially affect the results of the DDO RV program because its influence on *positions* of BF peaks was small. However, for the *line-strength* determination, the roles of rectification and the pseudo-continuum positioning are essential. The spectra do not provide any information on the pseudo-continuum shifts nor on errors in approximating pseudo-continua by broken lines; these shifts do not show up in the scatter of the measured values of the BF integrals S nor in the scatter of the δ shifts. In fact, the δ shifts for individual objects were found to be surprisingly similar with
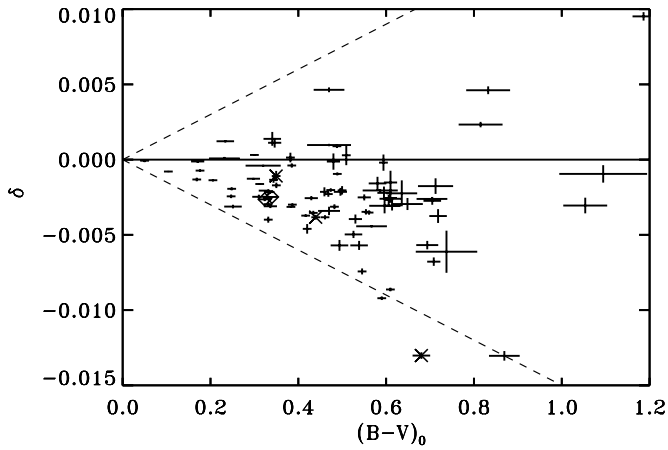
Figure 16. Measured values of the BF baseline shifts δ with their formal measurement errors shown by vertical error bars. The $(B - V)_0$ colors (Section 4) with their uncertainties are shown by horizontal bars. The broken lines give the adopted maximum range of δ for estimates of the log S dominant systematic errors ϵ_2 (Appendix A.3). Two detached binaries are marked by the over-plotted diamonds while three triple systems with $L_3/L_{12} < 0.05$ are marked by the slanted-cross (X) symbols.

Figure 17. Three main sources of log S errors vs. $(B - V)_0$. The diamonds close to the lower margin show errors ϵ_1 corresponding to the orbital-phase scatter in the measured values of log S. The crosses in the uppermost sequence show the combined errors ϵ(log S) consisting of all five components, $\epsilon_1-\epsilon_5$, all added in quadrature; they are dominated by the systematic uncertainties in the continuum placement, ϵ_2 (linearly increasing with $B - V$, as described in the text) and the unknown gravity, ϵ_3 (broken line).

very small formal uncertainties. This was unexpected, but is explainable by the way the DDO spectra were reduced: each star was analyzed by one investigator within typically hours, at most days; he or she tended to use the same choices in the piece-wise approximation when joining the highest points of the pseudo-continuum. This resulted in similar *systematic* errors for all spectra of a given star. Thus, the values of average δ and of their scatter are almost meaningless for individual objects. However, the values of δ for the whole sample, by providing information of their spread between stars, can be still useful in a statistical sense: the observed *range* of δ can be used to estimate the expected *range* of Δ and thus the uncertainties of the integrals S entering through the corrections $(1 + \Delta)$.

The distribution of the individual values of δ versus the star colors is shown in Figure 16; we use there the de-reddened colors as these represent spectral complexity. The errors in the shifts δ are not the same across the whole range of effective temperatures: they are small for early-type binaries having spectra with few, weak lines, and are large for late-type spectra which even without rotational and orbital broadening show strong blending. There is a virtual absence of δ shifts for $B - V < 0.25$ and a rapid increase in their size for red stars. Most δ shifts are negative implying too low measured lines strengths for later spectral types. Note however the presence of a few *positive* values of δ indicating that the continuum was placed too high and that the shift was over-corrected.

The lines in Figure 16 give our adopted, rather generous estimate of the maximum range of δ as a function of the de-reddened color $(B - V)_0$: $\delta_{\max} = \pm 0.015 \max(0, (B - V)_0 - 0.1)$. The measured values of log S were corrected using: $\log S_{\rm corr} = \log S_{\rm meas} + \log(1 + C\delta)$. Although only in the idealized case of perfect rectification the two shifts would be proportional, $\Delta \simeq C\delta$, we nevertheless assumed such scaling. The multiplier C depends on the shape of the BF. Experiments with various shapes of BFs have led to $C = 12 \pm 3$. From now on, we will call log $S_{\rm corr}$ simply log S remembering that these values include the baseline level corrections. The corrections are not large; the largest for the sample was $|\log(1 + C\delta)| = 0.06$.

The systematic error of log S due to the assumed scatter in δ is the second uncertainty in the evaluated values of BF integrals:
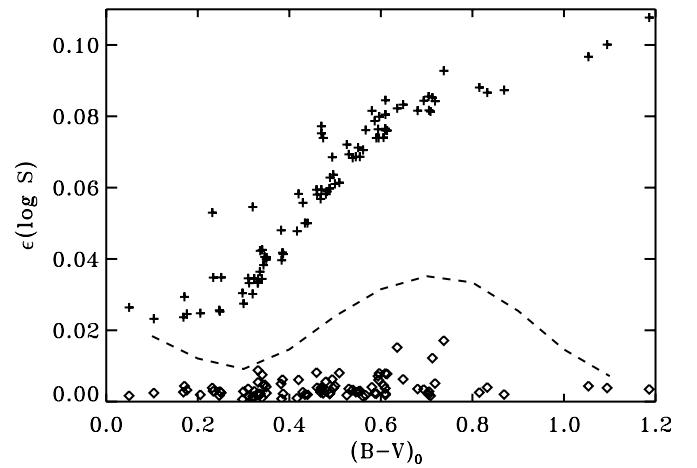
$\epsilon_2 = (C + 3) \, 0.015/2.3 \times \max(0, (B - V)_0 - 0.1)$; the coefficient C has been increased by 3 to account for its uncertainty. This error was added in quadrature to the random measurement errors ϵ_1. As detailed in Appendix A.3, ϵ_2 dominates in the final uncertainty budget.

A.2. Surface Gravity and the Synthetic $B - V$ Colors

We assumed that the gravities of most EW systems are approximately solar (i.e., $\log g_\odot = 4.44$ cgs) because the binaries are located along the main sequence and our previous luminosity class estimates were mostly consistent with the luminosity class V (dwarfs). The observed scatter in orbital periods (for a given effective temperature) reaching $\Delta \log P \simeq 0.2$ (Rucinski & Duerbeck 1997) suggests that there exists a corresponding scatter in gravities, but probably not exceeding a factor of about two, which is much less than the factor of 10 between the two model values of log g that we used. In the end, we used the differences in the theoretical values of log S between the two gravities, scaled to the difference $\Delta \log g = 0.3$. The median differences in log S (over all metallicities) range within $[-0.035, 0]$. We give them in the last column of Table 4. The absolute values of these differences are identified as the third uncertainty of log S. This uncertainty, ϵ_3, is entirely related to the use of the models and not to the observational values of S.

The differences in $\Delta(B - V)$, between the observed Bessell (1979) and our theoretical values represent an inherent (systematic) uncertainty in the models which constitute the fourth source of systematic error in log S: $\epsilon_4 = (\partial \log S_{\rm th}/\partial(B - V)) \times \Delta(B - V)$.

A.3. Summary of Uncertainty Estimates

Estimates of the errors of log S and their dependence on the color index are shown in Figure 17. In the summary below, the errors with index numbers all apply to log S and are non-dimensional, similarly to this quantity.

1. ϵ_1 (Appendix A.1). It is the *rms* error resulting from the orbital-phase scatter in the measured values of log S. It is deceptively small: the median is 0.0032, the maximum value 0.02. This is the only random error measured directly,

the remaining ones listed below are estimates of systematic errors. ϵ_1 is shown along the lower axis of Figure 17.

2. ϵ_2 (Appendix A.1). This uncertainty represents difficulties with continuum placement as they increase toward later spectral types. This is the dominant source of uncertainty. We assumed it to be linearly dependent on $B - V$; it reaches about 0.1 for $B - V = 1.0$ (see Figure 16). Although we assumed that ϵ_2 is symmetric around zero, the actual errors may have a skewed distribution with the dominance of negative values.

3. ϵ_3 (Section 5.1). This error is related to the use of the atmosphere models and describes lack on information on the actual values of gravity $\log g$. We used as error estimates 0.3 of the median differences (for all metallicities) between the model values for $\log g = 3.5$ and 4.5. This uncertainty reaches 0.035, as shown by the broken line in Figure 17.

4. ϵ_4 (Section 5.1). We found that our models differed systematically from the Bessell (1979) calibration (Figure 2). The resulting uncertainty of $\log S$ is the result of projecting the calibration differences $\Delta(B - V)$ into the model dependence of $\log S$ on the color index: $\epsilon_4 = (\partial \log S_{th}/\partial(B - V)) \times \Delta(B - V)$. For simplicity, we used the solar-metallicity dependence for the derivative.

5. ϵ_5 (Section 5.1). This is a similar dependence to above, but it projects the individual color uncertainties $\epsilon(B - V)$ (Section 4.1) into $\log S$. The same formula as above for ϵ_4 applies with the systematic trend $\Delta(B - V)$ replaced by the color uncertainty $\epsilon(B - V)$.

6. Three additional uncertainties in $\log S$ could not be characterized. They are expected to produce a systematic trend in the measured line strengths $\log S$ making them systematically too low for late spectral types. They result from: (a) a skewed distribution of ϵ_2 with dominant negative deviations (Appendix A.1), (b) our use of a single template across the spectral range, and (c) line emission filling-in the magnesium-triplet lines which—if present—would become more important for late spectral types (Appendix C). We detected such a trend and removed it using the Strömgren photometry index m_1 (Sections 6 and 7).

APPENDIX B

IS USE OF A SINGLE TEMPLATE JUSTIFIED?

As described above, we used one template spectrum of HD 128167 for determination of BFs for all observations and for all atmosphere models. The template served as an intermediate device for integration of information from the whole spectral window into just one number characterizing the total line strength for a given spectrum. This number was then averaged for all spectra and interpolated in the pre-computed two-dimensional table of the atmosphere-model BF strengths, $\log S = \log S(T_{eff}, [M/H])$, to determine the metallicity [M/H]. This was a simple and convenient approach; it by-passed the inherent problem of poorly known effective temperatures of our targets and permitted following temperature uncertainties as they propagated into uncertainties of [M/H].

The weakness of the above approach is that the BF method works perfectly well when the program and template spectra are identical and were taken at the same spectral resolution which controls how spectral lines are merged to define the pseudo-continuum. Because the spectra become richer at lower temperatures, more line blending occurs there even for sharp-line templates. This effect is missed when one template is used. This will not show up in any BF baseline shift (δ) because it is the template which would require modification, not the object spectra. The correct approach would be to use an individual template spectrum for each object, computed for the specific effective temperature and appropriately adjusted in spectral resolution to that of the observed spectrum. We did not follow this approach because we simply could not trust the available color measurements to provide correct effective-temperature estimates. We did not have sufficiently enough late-type template spectra to do tests on the dependence of the results on the template used. Some limited tests with another RV template that we used frequently, HD 65583 (G8V), confirmed the expected tendency for lowered values of S when the template is too early.

The assumption of a single template spectrum on the measured values of $\log S$ has the same sign as the effect of the pseudo-continuum rectification and resulting negative δ shifts, both should produce too low $\log S$ for later spectral types. One additional contribution in the same sense can come from chromospheric activity, as we describe in the next section. Because all these three tendencies could not be properly characterized, we dealt with the observed trend in the derived metallicities by relating our results to metallicities determined using the Strömgren photometry. This is described in Sections 5–7.

APPENDIX C

CAN PHOTOSPHERIC AND CHROMOSPHERIC ACTIVITY AFFECT STRENGTHS OF THE LINES?

The magnesium triplet was observed to be moderately filled-in by emission in spectra of solar flares by Acampa et al. (1982). Similar filling-in of the absorption lines was detected in the most chromospherically active stars (Waite et al. 2011). An artificial reduction in the depth of the magnesium lines would lead to reduced values of S and thus derivation of too low metallicity. As was discussed in Section 2.2, the magnesium-triplet lines contribute very little ($<10\%$) to the overall line strength S in the early-F type spectra which are dominated by iron lines. But the triplet contribution grows for later spectral types so that—if its lines are partly filled-in—the metallicity may be biased. We stress that we do not assume that activity increases for later spectral types; we only point out that the magnesium-triplet lines contribute more to the measured strengths $\log S$. The filling-in by emission cannot be determined from the EW binary spectra because there is no way of separating the magnesium lines from the multitude of rotationally blended iron lines in the spectral window.

While a large fraction of numerous reports of light curve asymmetries in EW binaries may manifest contact model deficiencies (Pribulla et al. 2011), some support for small, dark spots comes from spectroscopic BF profile observations (Barnes et al. 2004; Pribulla & Rucinski 2008). It is important to stress that as long as the spots are dark, they would not affect our metallicity analysis at all. This is because we use rectified spectra so that the line depths are relative to the total flux from the star, irrespectively of any flux reduction due to spots. The spots would influence our results only if they modified the observed colors (leading to wrong assumed T_{eff}) or contributed their own spectral signatures. While the former effect cannot be excluded (but would require a separate investigation of binaries with the definite presence of spots), the spectral signatures of spots are not expected to be detectable in low S/N spectra of the magnesium-triplet region. We note that detection of spot spectra

in active stars has so far been attempted using special techniques in application to molecular bands in the infrared region (O'Neal et al. 1998).

REFERENCES

Acampa, E., Smaldone, L. A., Sambuco, A. M., & Falciani, R. 1982, A&AS, 47, 485
Aumer, M., & Binney, J. J. 2009, MNRAS, 397, 1286
Barnes, J. R., Lister, T. A., Hilditch, R. W., & Collier Cameron, A. 2004, MNRAS, 348, 1321
Bessell, M. S. 1979, PASP, 91, 589
Bilir, S., Karatas, Y., Demircan, O., & Eker, Z. 2005, MNRAS, 357, 497
Blaauw, A., Tolbert, C. R., West, R. M., & Bartaya, R. A. 1976, A&AS, 23, 393
Budaj, J., Elkin, V., & Hubeny, I. 2005, in IAU Symp. 210, Modelling of Stellar Atmospheres, ed. N. Piskunov, W. W. Weiss, & D. F. Gray (Cambridge: Cambridge Univ. Press), poster E44
Castelli, F., & Kurucz, R. L. 2004, arXiv:astro-ph/0405087
Coskonoglu, B., Ak, S., Bilir, S., et al. 2011, MNRAS, 412, 1237
Crawford, D. L., & Barnes, J. V. 1970, AJ, 75, 946
Crawford, D. L., & Perry, C. L. 1966, AJ, 71, 206
Crawford, D. L., & Perry, C. L. 1976, PASP, 88, 454
D'Angelo, C., van Kerkwijk, M. H., & Rucinski, S. M. 2006, AJ, 132, 650
de Jong, J. T. A., Yanny, B., Rix, H.-W., et al. 2010, ApJ, 714, 663
Donati, J.-F., & Collier Cameron, A. 1997, MNRAS, 291, 1
Donati, J.-F., Semel, M., Carter, B. D., Rees, D. E., & Collier Cameron, A. 1997, MNRAS, 291, 658
Edvardsson, B., Andersen, J., Gustafsson, B., et al. 1993, A&A, 275, 101
Eggen, O. J. 1961, RGOB, 31, 101
Eggen, O. J. 1967, MmRAS, 70, 111
European Space Agency 1997, The Hipparcos and Tycho Catalogues (ESA SP-1200; Noordwijk: ESA)
Feltzing, S., & Bensby, T. 2009, in IAU Symp. 258, The Ages of Stars, ed. E. E. Mamajek, D. R. Soderblom, & R. F. G. Wyse (Cambridge: Cambridge Univ. Press), 23
Gazeas, K., & Niarchos, P. G. 2006, MNRAS, 370, L29
Gilmore, G., Randich, S., Asplund, M., et al. 2012, Msngr, 147, 25
Gilmore, G., & Reid, N. 1983, MNRAS, 202, 1025
Grundahl, F., Clausen, J. V., Hardis, S., & Frandsen, S. 2008, A&A, 492, 171
Guinan, E. F., & Bradstreet, D. H. 1988, in Formation and Evolution of Low Mass Stars, ed. A. K. Dupree & M. T. Lago (Dordrecht: Kluwer), 345
Hauck, B., & Mermilliod, M. 1998, A&AS, 129, 431
Hilditch, R. W., & Hill, G. 1975, MmRAS, 75, 101
Holmberg, J., Nordström, B., & Andersen, J. 2009, A&A, 501, 941
Hrivnak, B. J. 1989, ApJ, 340, 458
Hubeny, I., & Lanz, T. 1995, ApJ, 439, 875
Johnson, H. L., & Morgan, W. W. 1951, ApJ, 114, 522
Jordi, C., Figuearas, F., Torra, J., & Asiain, R. 1996, A&AS, 115, 401
Kaluzny, J., & Rucinski, S. M. 1993, in ASP Conf. Ser. 53, Blue Stragglers, ed. R. A. Saffer (San Francisco, CA: ASP), 164
Kaminski, K. Z., Rucinski, S. M., Matthews, J. M., et al. 2007, AJ, 134, 1206
Klemola, A. R. 1977, PASP, 89, 402
Kreiner, J. M. 1977, in Proc. IAU Colloq. 42, The Interaction of Variable Stars with Their Environment, ed. R. Kippenhahn, J. Rahe, & W. Strohmeier (Bamberg: Remeis-Sternwarte), 393
Krtička, J. 1998, in Proc. 29th Stellar Conference on Variable Star Research, ed. J. Dušek & M. Zejda (Brno: Nicholas Copernicus Observatory and Planetarium), 73
Kubiak, M., Udalski, A., & Szymanski, M. 2006, AcA, 56, 253
Lallement, R., Walsh, B. Y., Vergely, J. L., Crifo, F., & Sfeir, D. 2003, A&A, 411, 447
Leroy, J. L. 1999, A&A, 346, 955
Lindegren, L., Babusiaux, C., Bailer-Jones, C., et al. 2008, in IAU Symp. 248, A Giant Step: From Milli- to Micro-arcsecond Astrometry (Cambridge: Cambridge Univ. Press), 217
Lu, W., & Rucinski, S. M. 1993, AJ, 118, 515
Lu, W., & Rucinski, S. M. 1999, AJ, 106, 361
Lu, W., Rucinski, S. M., & Ogloza, W. 2001, AJ, 122, 402
Lucy, L. B. 1968a, ApJ, 151, 1123
Lucy, L. B. 1968b, ApJ, 153, 877
Lucy, L. B. 1976, ApJ, 205, 208
Maciejewski, G., & Ligeza, P. 2004, IBVS, 5504

Martinez-Arnaiz, R., Maldonado, J., Montes, D., Eiroa, C., & Montesinos, B. 2010, A&A, 520A, 79
Mochejska, B. J., Stanek, K. Z., Sasselov, D. D., & Szentgyorgyi, A. H. 2002, AJ, 123, 3460
Mochejska, B. J., Stanek, K. Z., Sasselov, D. D., et al. 2005, AJ, 129, 2856
Mochnacki, S. W. 1981, AJ, 245, 650
Oegerle, W. R., Jenkins, E. B., Shelton, R. L., Bowen, D. V., & Chayer, P. 2005, ApJ, 622, 377
Olsen, E. H. 1983, A&AS, 54, 55
Olsen, E. H. 1993, A&AS, 102, 89
Olsen, E. H. 1994, A&AS, 106, 257
O'Neal, D., Neff, J. E., & Saar, S. H. 1998, ApJ, 507, 919
Perry, C. L., & Johnston, L. 1982, ApJS, 50, 451
Pinnsonneault, M. H., Terndrup, D. M., Hanson, R. B., & Stauffer, J. R. 2004, ApJ, 600, 946
Pribulla, T., & Rucinski, S. M. 2006, AJ, 131, 2986
Pribulla, T., & Rucinski, S. M. 2008, MNRAS, 386, 377
Pribulla, T., Rucinski, S. M., Blake, R. M., et al. 2009a, AJ, 137, 3655
Pribulla, T., Rucinski, S. M., Conidis, G., et al. 2007, AJ, 133, 1977
Pribulla, T., Rucinski, S. M., DeBond, H., et al. 2009b, AJ, 137, 3646
Pribulla, T., Rucinski, S. M., Kuschnig, R., Ogloza, W., & Pilecki, B. 2009c, MNRAS, 392, 847
Pribulla, T., Rucinski, S. M., Lu, W., et al. 2006, AJ, 132, 769
Pribulla, T., Vaňko, M., Chochol, D., Hambálek, L., & Parimucha, Š 2011, AN, 332, 607
Pych, W., Rucinski, S. M., DeBond, H., et al. 2004, AJ, 127, 1712
Reid, I. N., Turner, E. L., Turnbull, M. C., Mountain, M., & Valenti, J. A. 2007, ApJ, 665, 767
Rucinski, S. M. 1983, A&A, 127, 84
Rucinski, S. M. 1992, AJ, 104, 1968
Rucinski, S. M. 1998a, AJ, 115, 1135
Rucinski, S. M. 1998b, AJ, 116, 2998
Rucinski, S. M. 2000, AJ, 120, 319
Rucinski, S. M. 2002, AJ, 124, 1746
Rucinski, S. M. 2006, MNRAS, 368, 1319
Rucinski, S. M. 2010a, in ASP Conf. Ser. 435, Binaries–Key to Comprehension of the Universe, ed. A. Prša & M. Zejda (San Francisco, CA: ASP), 195
Rucinski, S. M. 2010b, in AIP Conf. Proc. 1314, International Conf. on Binaries: In Celebration of Ron Webbink's 65th Birthday (Melville, NY: AIP), 29
Rucinski, S. M. 2012, in IAU Symp. 282, From Interacting Binaries to Exoplanets: Essential Modeling Tools, ed. M. Richards & I. Hubeny (Cambridge: Cambridge Univ. Press), 365
Rucinski, S. M., Capobianco, C. C., Lu, W., et al. 2003, AJ, 125, 3258
Rucinski, S. M., & Duerbeck, H. W. 1997, PASP, 109, 1340
Rucinski, S. M., & Kaluzny, J. 1981, AcA, 31, 409
Rucinski, S. M., & Lu, W. 1999, AJ, 118, 2451
Rucinski, S. M., & Lu, W. 2000, MNRAS, 315, 587
Rucinski, S. M., Lu, W., Capobianco, C. C., et al. 2002, AJ, 124, 1738
Rucinski, S. M., Lu, W., & Mochnacki, S. W. 2000, AJ, 120, 1133
Rucinski, S. M., Lu, W., Mochnacki, S. W., Ogloza, W., & Stachowski, G. 2001, AJ, 122, 1974
Rucinski, S. M., & Pribulla, T. 2008, MNRAS, 388, 1831
Rucinski, S. M., Pribulla, T., Mochnacki, S. W., et al. 2008, AJ, 136, 586
Rucinski, S. M., Pribulla, T., & van Kerkwijk, M. H. 2007, AJ, 134, 2353
Rucinski, S. M., Pych, W., Ogloza, W., et al. 2005, AJ, 130, 767
Schlegel, D. J., Finkbeiner, D. P., & Davis, M. 1998, ApJ, 500, 525
Schmidt, E. G. 1976, PASP, 88, 63
Schönrich, R., & Binney, J. 2009, MNRAS, 399, 1145
Schroder, C., Reiners, A., & Schmitt, J. H. M. M. 2009, A&A, 493, 1099
Seabroke, G. M., & Gilmore, G. 2007, MNRAS, 380, 1348
Siwak, M., Zola, S., & Koziel-Wierzbowska, D. 2010, AcA, 60, 305
Skrutskie, M. F., Cutri, R. M., Stiening, R., et al. 2006, AJ, 131, 1163
Stepien, K. 2006, AcA, 56, 199
Stepien, K. 2009, MNRAS, 397, 857
Strömgren, B. 1966, ARA&A, 4, 433
Terrell, D., Gross, J., & Cooney, W. R., Jr. 2012, AJ, 143, 99
Valenti, J. A., & Fischer, D. A. 2005, ApJS, 159, 141
van Leeuwen, F. 2007, Hipparcos, the New Reduction of the Raw Data (Berlin: Springer)
Veltz, L. O., Bienayme, O., Freeman, K. C., et al. 2008, A&A, 480, 753
Waite, I. A., Marsden, S. C., Carter, B. D., et al. 2011, PASA, 28, 323
Weistrop, D. 1972, AJ, 77, 366
Wielen, R. 1977, A&A, 60, 263